Communications Biology

https://doi.org/10.1038/s42003-025-09447-0

Article in Press

Dietary methionine deprivation enhances renal resilience against ischemia-reperfusion injury in mice through modulation of glucose oxidation

Received: 11 December 2024

Accepted: 18 December 2025

Cite this article as: Peng, X., Xie, Y., Pan, H. *et al.* Dietary methionine deprivation enhances renal resilience against ischemia-reperfusion injury in mice through modulation of glucose oxidation. *Commun Biol* (2025). https://doi.org/10.1038/s42003-025-09447-0

Xiaofeng Peng, Yuanhao Xie, Hao Pan, Tianxin Ma, Yaoling Zou, Qun Su, Jianghua Chen, Hong Jiang & Cunqi Ye

Dietary methionine deprivation enhances renal resilience against ischemia-reperfusion injury in mice through modulation of glucose oxidation

Authors

Xiaofeng Peng[1,10], Yuanhao Xie[2,10], Hao Pan[3], Tianxin Ma[4], Yaoling Zou[5], Qun Su[6], Jianghua Chen[1], Hong Jiang[1]*, Cunqi Ye[1,7,8,9]*

Affiliations

[1]Kidney Disease Center, The First Affiliated Hospital, Zhejiang University School of Medicine, Hangzhou, China

[2]Department of Orthopedic Surgery, The Second Affiliated Hospital of Zhejiang University, 310058, Hangzhou, Zhejiang, China

[3]Department of Urology, The First Affiliated Hospital, College of Medicine, Zhejiang University, Hangzhou, Zhejiang, China

[4]National R&D Center for Freshwater Fish Processing, Jiangxi Normal University, Nanchang, 330022, China

[5]Hangzhou Shangcheng District Women and Children's Health Service Center, Hangzhou, China

[6]Critical Care Medicine Department, The First Affiliated Hospital, College of Medicine, Zhejiang University, Hangzhou, China.

[7]Zhejiang Provincial Key Laboratory for Cancer Molecular Cell Biology, Life Sciences Institute, Zhejiang University, Hangzhou, China

[8]Department of Reproductive Endocrinology, Women's Hospital, Zhejiang University School of Medicine, Zhejiang, Hangzhou, China

[9]Hainan Institute, Zhejiang University, Sanya, China

[10]These authors contributed equally to this work.

*Corresponding authors:

Hong Jiang, jianghong961106@zju.edu.cn; Cunqi Ye, yecunqi@zju.edu.cn

Abstract

Renal ischemia-reperfusion injury (IRI) is a leading cause of acute kidney injury (AKI) and presents significant challenges during kidney transplantation. Due to the detrimental effects of IRI on kidney function and the lack of effective intervention strategies, we conduct a multi-omics study in male mice with surgically induced renal IRI, revealing a modulatory role for the metabolite S-adenosylmethionine (SAM) in AKI development. Our metabolic analysis of clinical samples establishes a link between various AKI conditions and marked elevations in serum SAM, underlying its potential as a biomarker for diagnosis. Furthermore, we find that short-term dietary methionine deprivation, which reduces circulating methionine and kidney SAM levels, effectively enhances renal resilience against IRI. In vivo isotopic tracing demonstrates that this diet preconditions kidney metabolic programs, enhancing glucose and fatty acid oxidation in preparation for IRI. Particularly, the activation of pyruvate dehydrogenase, which produces acetyl-CoA to fuel the tricarboxylic acid (TCA) cycle, highlights an energy-efficient strategy of glucose metabolism that is essential for the protective effects of dietary methionine deprivation.

Introduction

Acute kidney injury (AKI) is a clinical syndrome characterized by the sudden loss of kidney function, often triggered by ischemia, nephrotoxins, or sepsis[1]. AKI is also common observed in kidney donors and recipients, posing a significant risk to the success of renal transplantation. Despite progress in understanding the mechanisms of AKI—including renal microvascular injury, endoplasmic reticulum stress, mitochondrial dysfunction, cell death, impaired autophagy, inflammation, and maladaptive repair[2-6]—effective therapeutic interventions remain lacking. Current treatments are limited to supportive care, such as fluid management and renal replacement therapy, without targeted therapies to prevent or reverse AKI[7]. AKI is associated with high morbidity and mortality, affecting 10-15% of hospitalized patients and more than 50% of those in intensive care units[8-10]. This significant clinical burden underscores the urgent need for early detection methods and novel interventions to reduce mortality and long-term complications.

The kidney has a high metabolic demand and limited capacity to regulate blood flow, making them particularly vulnerable to injury[11,12]. As the most abundant and metabolically active cells in the kidney, proximal tubular epithelial cells (TECs) play a critical role in reabsorbing electrolytes and nutrients. These cells are often the primary targets of various insults, which can lead to substantial and sometimes irreversible kidney damage[13,14]. Although direct in vivo metabolic flux studies of the kidney are scare, gene expression and metabolite analyses suggest that disruptions in glucose metabolism and fatty acid oxidation (FAO) are key contributors to kidney injury[15]. Under normal conditions, TECs primarily rely on FAO for energy production[16,17]. During AKI, TECs shift toward glycolysis and the pentose phosphate pathway[18-21]. Recovery from AKI restores FAO and enhances glucose oxidation to support tissue regeneration[17,22]. Dysregulation of these metabolic pathways may predispose TECs to apoptosis and dedifferentiation, further contributing to lipotoxicity and kidney damage[15]. Therefore, pharmaceutical or nutraceutical interventions targeting renal metabolism to adapt to AKI-induced metabolic shifts may offer a promising strategy to mitigate kidney damage[23].

Dietary interventions, such as protein restriction, are commonly used in managing chronic kidney disease, as low-protein diets can constrict afferent arterioles to reduce glomerular injury[24]. In mice, calorie restriction has also been shown to protect against AKI by enhancing insulin sensitivity, reducing inflammation, modulating energy metabolism, and boosting antioxidant defense[25-31]. Despite the potential practical value of dietary interventions, especially in preventing AKI in renal transplantation, their clinical application remains limited largely due to inconsistent outcomes in diverse patient populations[32]. A primary limitation is the lack of mechanistic insight into how these dietary interventions modulate metabolism at the physiological level. Thus, understanding the common dysregulation underlying various forms of AKI, as well as mechanisms through which dietary restriction improves these metabolic phenotypes, is essential for translating dietary strategies into effective patient care.

In this study, we employed a multi-omics approach to systemically profile transcriptomics, proteomics, and metabolomics in an AKI mouse model established by surgical induction of renal ischemia-reperfusion injury (IRI). Our analysis revealed that dysregulation of SAM metabolism is a key feature of AKI, with consistently elevated serum SAM levels observed across various AKI conditions, including two human patient cohorts. This suggests that SAM may serve as a potential biomarker for AKI diagnosis. These findings prompted us to investigate dietary methionine restriction (MR) as an intervention to alleviate kidney damage during AKI. Remarkably, a 7-day methionine-free (MF) diet provided significant protection against IRI-induced kidney damage in mice. In vivo stable isotope tracing showed that this short-term dietary intervention enhanced both glucose and fatty acid oxidation in the kidney, highlighting key metabolic processes for renal protection. Further chemical interventions demonstrated that modulation of glucose oxidation, rather than FAO, is crucial for the protective effects of the MF diet. Specifically, activation of pyruvate dehydrogenase, which enhances glucose oxidation by fueling acetyl-CoA into the TCA cycle, replicates the protective effects of methionine deprivation. In summary, our findings suggest that dietary MR and chemical activation of glucose oxidation may serve as promising metabolic strategies to mitigate AKI.

Results

Multi-omics analyses reveal systemic changes in kidney metabolism in response to renal IRI

To systemically investigate metabolic and regulatory dysregulation in AKI, we established an AKI mouse model by surgically induced renal IRI (Fig. 1a). As expected, renal function impairment was evident 24 hours post-surgery in 8-week-old adult male C57BL6/J mice, indicated by significant elevations in blood urea nitrogen (BUN) and serum creatinine (sCr) levels compared to the sham group (Supplementary Fig.1a-b). We then performed multi-omics analyses including RNA sequencing (RNA-seq), quantitative proteomics, and targeted metabolomics on mouse kidney tissues (Supplementary Fig. 1c). This approach yielded a comprehensive dataset comprising 31,582 analytes, including 24,522 transcripts, 6,942 proteins, and 118 metabolites (Supplementary Fig. 1c and Supplementary Data 1). Of these, 10,350 analytes (32.8% of the total analytes, $p < 0.05$) displayed significant changes across all omics layers. Notably, transcriptional and metabolic alterations were most pronounced, with 39.5% of genes and 60.2% of measured metabolites exhibiting significant responses to renal IRI. (Fig. 1b). Extensive changes at omic levels were also observed in other AKI studies[33-36].

We next conducted gene ontology (GO) analysis and found significant enrichment of differentially expressed transcripts and proteins associated with the upregulation of apoptosis and inflammatory response (Fig. 1c-d). This is consistent with the activation of renal cell death and protective mechanisms typically observed in AKI kidneys[37-39]. KEGG (Kyoto Encyclopedia of

Genes and Genomes) pathway analysis of differential metabolites showed a pronounced upregulation in pathways involving nitrogenous metabolites, such as amino acid biosynthesis and purine metabolism (Fig. 1e). Notably, these same metabolic pathways exhibited contrasting downregulation at the transcriptional and protein levels (Fig. 1c-d). These omics results collectively underscore the disruptive nature of nitrogen metabolism in kidney injury, highlighting the complex regulatory feedback between transcription, protein expression, and metabolic pathways.

To further elucidate the signature metabolic features in IRI kidneys, we performed gene set enrichment analysis (GSEA) of the transcriptome data. We observed significant upregulation in pathways related to hypoxia and apoptosis (Fig. 1f), which is expected given the limited oxygen and metabolic supply in ischemic kidneys[40,41]. Interestingly, pathways involving mitochondrial activities, such as the TCA cycle, oxidative phosphorylation, and FAO were downregulated (Fig. 1f), suggesting that these mitochondria-centered metabolic changes are functional responses to renal IRI[42].

Finally, we performed an integrated network analysis of the transcriptomic, proteomic, and metabolomic data to identify specific metabolites of interest. This analysis highlighted S-adenosylmethionine (SAM) as a key node with the highest degree of centrality (Fig. 1g and Supplementary Data 1). In addition, KEGG enrichment revealed that pathways related to lipid metabolism (e.g., fatty acid degradation, phospholipase D signaling and glycosphingolipid biosynthesis) and glucose metabolism (e.g., pyruvate metabolism) were among the most significantly altered between IRI and sham kidneys. The confluence of these dysregulated pathways suggests that SAM accumulation is central to the AKI-associated metabolic rewiring, providing a direct justification for subsequent dietary interventions. Notably, both SAM and its precursor, methionine, were significantly elevated in kidney tissues collected 24 hours post-IRI, confirming dysregulation in SAM metabolism (Fig. 1h).

The kidney is a SAM-consuming organ

To further investigate the disruption of SAM metabolism in renal IRI, we analyzed circulating levels of SAM, along with its immediate upstream and downstream metabolites, methionine and S-adenosylhomocysteine (SAH). In the IRI-induced AKI group, we observed a 46% decrease in serum methionine levels and an over 7-fold increase in SAM levels compared to the sham group (Fig. 2a). A similar pattern of reduced methionine and elevated SAM levels was observed in another AKI model induced by cisplatin treatment (Fig. 2b), where kidney injury was evidenced by increases in BUN and sCr levels, as well as extensive tubular dilation and necrosis, and cast formation (Supplementary Fig. 1d-g). These findings suggest that the kidney, as a metabolically active organ, substantially consumes SAM. Upon kidney injury, the inability to effectively dispose of SAM leads to its accumulation in circulation, indicating that elevated SAM may serve as a biomarker for AKI.

SAM elevation in AKI patients

To validate whether SAM elevation is a consistent metabolic signature of AKI in humans, we analyzed serum samples from two different patient cohorts with AKI. In these clinical studies, we matched patients for demographic and clinical characteristics, including age, gender, and chronic disease conditions (Supplementary Data 1). In the sepsis cohort, we examined 18 patients with AKI and 32 without, finding that sepsis patients with AKI exhibited an average 4-fold increase in serum SAM levels, along with a significant rise in SAH (Fig. 2c). Similarly, in the cardiac surgery cohort, we analyzed 34 with AKI and 36 without, where serum SAM and SAH levels showed average increases of 2-fold and 1.4-fold, respectively (Fig. 2d). These patient data reinforce the notion that SAM accumulation in circulation is a conserved metabolic response to AKI, reflecting a critical SAM consumption in the kidney.

Elevated serum SAM levels do not exacerbate kidney dysfunction

To determine whether elevated serum SAM levels contribute to worsening kidney function, we utilized transgenic mice (*Pemt* $^{-/-}$)(Fig. 2e), designed to promote circulating SAM levels, and examined their BUN and sCr levels 24 hours after surgical induction of AKI. The liver, as the primary organ for SAM production, plays a crucial role in maintaining systemic SAM homeostasis, with PEMT-mediated phospholipid methylation in hepatocyte being a key consumer of SAM[43,44]. Serum SAM levels increased by approximately 3-fold in *Pemt* $^{-/-}$ mice (Fig. 2f). However, despite this increase, SAM levels post-IRI in these mice were comparable to those in WT mice (Fig. 2f). Furthermore, there were no significant differences in BUN (Fig. 2g) and sCr (Fig. 2h) levels, or in renal histology (Supplementary Fig. 1h-i), between WT and *Pemt* $^{-/-}$ mice subjected to renal IRI.

These results suggest that elevated serum SAM levels are more likely a consequence of kidney injury, rather than a direct cause.

To definitively rule out SAM as a pathogenic driver, we directly tested the impact of supraphysiological SAM elevation on renal IRI through exogenous administration. Mice received intraperitoneal SAM or PBS twice during the 7-day CD diet prior to IRI (Fig. 2i). This intervention induced a robust >20-fold increase in serum SAM compared to PBS controls (Fig. 2j). Crucially, despite this profound SAM elevation, renal dysfunction was not exacerbated, as evidenced by comparable BUN (Fig. 2k) and sCr (Fig. 2l) levels between groups. This evidence, consistent with our genetic model (Fig. 2g-h), conclusively demonstrates that SAM accumulation is a biomarker of metabolic disruption rather than a mediator of kidney damage.

To further evaluate this diagnostic potential of serum SAM, we determined the kinetics of its increase following the IR (Fig. 2m). Strikingly, serum SAM exhibited a rapid induction with a significant 3.5-fold increase within just 30 minutes post-reperfusion, progressing to 5.4-fold after 120 minutes (Fig. 2n). This early elevation demonstrated accelerated kinetics compared to BUN (Supplementary Fig. 1j) and exhibited temporal dynamics parallel to sCr (Supplementary Fig. 1k), while significantly anticipating kidney tubular injury marker upregulation (NGAL/KIM1 protein expression; Supplementary Fig. 1l). Notably, serum SAM showed strong positive correlations with BUN ($r^2=0.63$, $p<0.005$) and sCr ($r^2=0.89$, $p<0.001$) during this acute phase (Fig. 2o-p), establishing serum SAM as one of the earliest detectable biomarkers of AKI.

MF diet mitigates IR-induced kidney injury

Although *Pemt* $^{-/-}$ mice with elevated serum SAM levels demonstrated similar vulnerability to AKI as WT mice, we investigated whether limiting SAM availability through restricting dietary methionine could precondition the kidney for metabolic adaptation, thereby mitigating renal damage from IRI. To test this idea, we fed adult male mice three different diets: normal methionine (CD, 0.86%), low methionine (MR, 0.17%), and methionine-free (MF, 0%) diets for 7 days prior to IRI surgery (Fig. 3a). Following this dietary regimen, mice on the MF diet exhibited moderate weight loss (Fig. 3b), without significant difference in calorie intake compared to the other two groups (Fig. 3c). Mice on normal or low methionine diets showed no weigh changes, despite a slight increase in calorie intake in the low methionine group (Fig. 3b-c). Notably, only the MF diet significantly reduced serum methionine levels after this short-term dietary intervention (Fig. 3d).

Consistent with the reduction in serum methionine levels, the 7-day MF diet conferred substantial protection against IRI-induced injury, with BUN levels nearly normalized and sCr reduced by 70% (Fig. 3e-f). In contrast, the low methionine diet did not provide adequate protection, as elevations in BUN and sCr levels were similar to those observed in mice fed the normal diet (Supplementary Fig. 2a-b). Metabolite analysis revealed that the MF diet resulted in approximately 40% reductions in kidney SAM levels (Fig. 3g). Furthermore, consistent with serum SAM as a potential biomarker for AKI, IRI-induced elevated serum SAM levels were normalized by the MF diet (Fig. 3h).

We next examined the mouse kidneys to further evaluate the protective effects of the MF diet. Notably, kidney size and weight decreased in the MF diet group, while kidney-to-body weight ratios remained unchanged (Supplementary Fig. 2c-d). Hematoxylin and eosin (HE) staining of kidney sections showed marked tubule necrosis in the outer stripe of outer medulla in post-IRI mice fed the normal diet (Fig. 3i) and the low methionine diet (Supplementary Fig. 2e-f), indicative of severe renal injury following IRI. This injury was significantly lowered in the MF diet group, with reduced tubular epithelial necrosis observed (Fig. 3i-j). Immunostaining for Lipocalin 2 (LCN2), a marker of kidney injury, showed minimal LCN2-positive renal cells in the MF diet group (Fig. 3k-l). Consistently, kidney injury markers LCN2 and kidney injury molecule 1 (KIM-1) were undetectable by western blot analysis in this group (Fig. 3m). These results further confirm that the 7-day MF diet provides substantial renal protection against IRI.

Given that MR can cause liver stress and potentially contribute to fatty liver progression[45,46], we evaluated liver function by measuring serum alanine aminotransferase (ALT) and aspartate aminotransferase (AST) activity levels in IRI mice under dietary treatment. Both ALT and AST activities significantly increased 24 hours post-IRI, indicating liver dysfunction (Fig. 3n-o). The MF diet slightly reduced ALT activity but had no effect on AST activity (Fig. 3n-o). These findings suggest that short-term methionine deprivation provides specific protection to the kidney without exacerbating liver function.

MF diet reduces triacylglycerol accumulation under IRI

The kidney has high energy demands, typically met through FAO in renal TECs. During AKI, a metabolic shift occurs toward glycolysis, accompanied by a temporary repression of FAO[15,22,36] (Fig. 4a). While this repression of FAO can lead to lipid dysregulation and lipotoxicity in the kidney[17,47], it remains unclear whether an MF diet can modulate FAO to alleviate metabolic stress during renal IRI.

To investigate the effects of IRI and dietary influences on renal lipid metabolism, we performed Oil Red O staining of kidney tissues. We found increased staining of neutral lipids post-IRI, which was significantly reduced in the MF diet group (Fig. 4b-c). To confirm this finding, we conducted lipidomics analysis using mass spectrometry. The volcano plot revealed evident increases in the levels of various of triacylglycerol (TAG) species under IRI (Fig. 4d), highlighting a dominant dysregulated feature of lipid metabolism in IRI kidneys. Specifically, there was a 15-fold increase in total renal TAG levels under IRI, which was reduced by 50% in mice fed the 7-day MF diet (Fig. 4e). Notably, TAG accumulation post-IRI was characterized by TAG species containing acyl chains of varying lengths and degrees of unsaturation, whereas the MF diet primarily affected TAG species with a total acyl carbon count of 40 to 52 (Fig. 4f).

To determine whether this dietary modulation of TAG levels reflected the response of TECs to IRI, we performed transmission electron microscopy in kidney tissues to assess the abundance and size of lipid droplets (LDs), which serve as cellular reservoirs for TAG. In line with the results from Oil Red O staining and lipidomics, the emergence of LDs within TECs post-IRI was significantly suppressed in mice fed the MF diet, evidenced by reductions in both the quantity and size of LDs (Fig. 4g-h).

MF diet enhances FAO, but may not be sufficient for renal protection against IRI

Because the observed accumulation of neutral lipids post-IRI aligns with the repression of FAO[48,49], we reasoned whether the dietary repression of IRI-induced TAG levels lies in an enhanced FAO. To test this, we conducted in vivo isotope tracing experiments using [U-^{13}C16] palmitate. Isotopic steady-state was achieved within 2.5 hours according to established protocols[50,51] (Fig. 4i), with comparable serum [U-^{13}C16] palmitate enrichment and relative abundance (Supplementary Fig. 3a-b), confirming similar tracer delivery. We then collected kidney tissues for analysis of palmitate-derived metabolites with ^{13}C labeling using mass spectrometry (Fig. 4j). We found that mice on the MF diet exhibited higher levels of m+16 palmitoyl-CoA (Fig. 4k) and m+16 palmitoylcarnitine (Fig. 4l), implying an increased activity of the carnitine palmitoyltransferase system, which is crucial for transporting long-chain acyl-CoAs into mitochondria for FAO. Given that FAO generates acetyl-CoA to fuel the TCA cycle, enhanced FAO should correlate with elevated levels of m+2 labeled TCA metabolites derived from infused [U-^{13}C16] palmitate (Fig. 4j). Indeed, the abundances of m+2 fumarate, m+2 glutamate, and m+2 glutamine (the latter two metabolites derived from α-ketoglutarate) significantly increased in the kidneys of mice on the MF diet (Fig. 4m and Supplementary Fig. 3c-d). Therefore, the results from the [U-^{13}C16] palmitate-based flux experiment confirm that FAO is enhanced after the 7-day MF diet.

To examine whether the enhancement of FAO from the MF diet contributes to renal protection against IRI, we administered etomoxir, a widely used inhibitor of carnitine palmitoyltransferase, to block FAO (Fig. 4n). Specifically, two doses of etomoxir were administered intraperitoneally to mice on the MF diet, 24 hours before and on the day of renal IRI (Fig. 4o), while kidney function was monitored by measuring BUN and sCr levels. We found that TAG levels significantly increased following etomoxir administration (Fig. 4p), indicating an effective blockage of FAO. If FAO enhancement were indeed a key factor in the protective effects of the MF diet, we anticipated that etomoxir-imposed FAO blockage would negate these benefits. However, contrary to our expectations, etomoxir treatment did not diminish the protective benefits observed in mice on the MF diet, as post-IRI BUN and sCr levels remained unchanged (Fig. 4q-r). These findings suggest that the enhancement of FAO from the MF diet is dispensable for renal protection against IRI, indicating that other metabolic mechanisms may be involved in the observed protective effects.

In vivo isotope tracing reveals enhanced glucose utilization in the kidney of mice on the MF diet

Given that another notable metabolic shift during IRI lies in glucose metabolism, we investigated whether dietary methionine availability could alter glucose utilization and whether this modulation contributes to the observed renal protection. To access this, we first performed in vivo stable isotope tracing by intravenously infusing [U-^{13}C6] glucose 24 hours post-surgery (Sham or IRI) (Fig. 5a). A continuous infusion of [U-^{13}C6] glucose at a rate of 0.1 μl/min/gBW for 2.5 hours was sufficient to achieve isotopic steady-state labeling[51]. Despite the predicted ethical safety of this low-dose, slow-rate infusion procedure[51-54], we noted a high incidence of loss of viability in IRI mice on the normal diet, contrasting sharply with survival rates in both the sham group and IRI mice on the MF diet (Fig. 5b). This increased mortality in the normal diet group likely results from fluid administration exacerbating renal burden, leading to multi-organ dysfunction[55,56]. The enhanced survival of IRI mice on the MF diet strongly indicates an overall improvement in metabolic fitness.

We then measured both labeled and unlabeled glucose in the serum and kidneys of the surviving mice 24 hours post-IRI after the 2.5-hour of [U-^{13}C6] glucose. After the continuous infusion of [U-^{13}C6] glucose, we observed similar amounts of fully labeled glucose in circulation across all four groups (Fig. 5c), indicating a sufficient and steady supply. Notably, serum ^{13}C6-glucose enrichment increased post-IRI and further rose with MF feeding (Supplementary Fig. 4a). Interestingly, compared to the normal diet, the amounts of unlabeled glucose in circulation significantly decreased in mice on the MF diet, which were further lowered with the IRI operation (Fig. 5d). As a result, the fractional levels of unlabeled glucose relative to total glucose in serum were reduced by both IRI and the MF diet (Fig. 5e). These fractional levels of unlabeled glucose reflect the turnover of residual unlabeled glucose under [U-^{13}C6] glucose infusion, as an indicator of glucose utilization. The facilitated turnover of glucose in circulation thus suggests increased utilization of glucose by the body, likely attributable to enhanced glucose uptake or metabolism in the kidney under these conditions.

In kidney tissues, we noted that total renal glucose levels were significantly reduced in mice on the MF diet, while fully labeled glucose levels increased in IRI mice on the normal diet (Fig. 5f). Renal $^{13}C6$-glucose enrichment mirrored circulatory patterns with significant elevation in MF-IRI group (Supplementary Fig. 4b). Further analysis revealed that the fractional levels of unlabeled glucose decreased in both the IRI and MF diet groups (Fig. 5g), exhibiting a similar pattern to their fractional levels in circulation (Fig. 5e). Therefore, in the kidneys subjected to IRI or the MF diet, glucose utilization was indeed increased. However, the sharp difference in renal glucose availability between the dietary groups suggests that the diet and IRI may have different impacts on glucose metabolism in the kidney.

Renal IRI leads to an increase in glycolytic flux to support lactate fermentation, independent of dietary treatment

To gain further insights into renal glucose metabolism in vivo, we developed a multiple reaction monitoring (MRM)-based, high-sensitivity mass spectrometry method to investigate stable isotope-labeled metabolites from kidney tissues infused with [U-$^{13}C6$] glucose. These metabolites are involved in glycolysis, fermentation, the TCA cycle, and cataplerotic pathways (Supplementary Fig. 4c). After surveying the abundances of all ^{13}C-isotopologues of these metabolites, we focused on those robustly detectable after the 2.5-hour [U-$^{13}C6$] glucose infusion experiment, including pyruvate, lactate, acetyl-CoA, fumarate, malate, glutamate, and glutamine (Supplementary Fig. 4c).

Consistent with IRI-induced glycolysis under hypoxia conditions[19,20], we observed increased production of m+3 lactate from infused [U-^{13}C6] glucose in the kidneys 24 hours post-IRI (Fig. 6a-b), further reflected by an elevated ratio of m+3 lactate to m+3 pyruvate levels (Fig. 6c-d). This accelerated lactate production by the fermentation of pyruvate sustains an increased glycolytic flux, which likely accounts for the facilitated glucose utilization in the IRI kidneys. Interestingly, mice on the MF diet, regardless of IRI surgery, exhibited increases in both m+3 lactate and m+3 pyruvate levels (Fig. 6b-c). Given that the MF diet resulted in a substantial reduction in renal glucose levels under a sufficient supply of [U-^{13}C6] glucose (Fig. 5f), the increased levels of labeled lactate and pyruvate suggest that the decrease in total renal glucose abundance was unlikely due to reduced uptake but rather to accelerated metabolism. However, IRI kidneys in both dietary groups displayed comparable increases in labeled lactate-to-pyruvate ratios (Fig. 6d), suggesting that other metabolic activities, rather than lactate fermentation, were responsible for the enhanced glucose consumption in the kidneys of mice on the MF diet.

The complete oxidation of glucose via the TCA cycle is impaired under IRI but effectively restored by the MF diet

To achieve more efficient energy production, pyruvate generated through glycolysis undergoes oxidative decarboxylation to form acetyl-CoA, which then enters the TCA cycle for complete glucose oxidation (Fig. 6e). We investigated whether the MF diet enhances the capacity of the TCA cycle for glucose oxidation. In IRI kidneys, mice on the normal diet exhibited a 67% reduction in m+2 acetyl-CoA levels, whereas this reduction was not observed in mice on the MF diet (Fig.

6f). Similarly, m+2 fumarate and m+2 malate levels were significantly reduced only in IRI mice on the normal diet, while levels in the MF diet group remained stable (Fig. 6g-h). In addition to m+2 TCA cycle metabolites generated after one round of the cycle, m+2 glutamate and m+2 glutamine, derived from cataplerotic pathways (Fig. 6e), were also elevated in the MF diet group (Supplementary Fig. 5a-b). Furthermore, metabolites such as glutamate, glutamine, and malate can be labeled in the m+3 form after the second round of the TCA cycle[57] (Fig. 6i), and we found that their levels were also significantly elevated in the MF diet group (Fig. 6j-l). Collectively, these findings strongly indicate that the MF diet can potently restore the reduction in acetyl-CoA production and the associated repression of the TCA cycle found in the IRI kidneys. Therefore, the glucose oxidation capacity enhanced by the MF diet likely better meets the energy demands required for kidney repair and regeneration[15], contributing to the improved renal resilience observed during IRI.

Chemical activation of pyruvate oxidation is sufficient to exert renal protection against IRI

To understand how the MF diet enhanced glucose oxidation in mouse kidneys, we analyzed quantitative proteomic data for metabolic enzymes involved in glycolysis and the TCA cycle (Fig. 7a). In kidney tissues collected 24 hours after the sham or IRI operation, we found that the MF diet modulated the levels of both glycolytic and TCA cycle enzymes (Fig. 7b). These complex changes likely shifted kidney glucose metabolism to favor oxidation for efficient energy production, thereby providing renal protection. Notably, we found decreases in TCA cycle enzyme levels associated with IRI, which were not restored by the MF diet (Fig. 7b). This suggests that the dietary modulation primarily influences glycolytic flux rather than affecting the TCA cycle at the protein level.

To enhance glucose oxidation, the production of acetyl-CoA through pyruvate dehydrogenase (PDH) catalysis must align with the increased pyruvate flux to entrain the TCA cycle. We hypothesized that modulating PDH activity could be a critical metabolic adaptation in mice on the MF diet (Fig. 7c). To test this, we administered dichloroacetate (DCA) to chemically activate PDH by inhibiting the PDH kinase (PDK). Mice subjected to either the MF diet or DCA in their drinking water for 7 days (Fig. 7d), and we compared the effects of both treatments against renal IRI. While DCA treatment did not impact body weight, food or water intake (Supplementary Fig. 6a-b), it exhibited renal protective effects similar to those on the MF diet. We observed evident reductions in BUN and sCr levels (Fig. 7e-f), along with decreased tubular injury as revealed by H&E staining of kidney tissues (Fig. 7g-h). Therefore, enhancing pyruvate oxidation is likely a crucial metabolic adaptation for renal protection against IRI.

Discussion

In this study, our integrated omics analysis highlights SAM as a central metabolite in AKI development. We establish a significant association between various AKI conditions and elevations in serum SAM, suggesting its potential as a valuable biomarker for AKI diagnosis. We modulate dietary methionine to further explore SAM-mediated metabolic adaptation within the kidney using an IRI mouse model. The implementation of a 7-day MF diet demonstrates substantial renal protective effects, characterized by notable enhancements in both glucose and fatty acid oxidation in the kidney, as revealed by in vivo isotopic tracing with [U-^{13}C6] glucose and [U-^{13}C16] palmitate. Importantly, our findings further indicate that the activation of PDH, which promotes glucose oxidation for energy production, is key to these protective effects. Therefore, rather than relying solely on FAO, the adaptive response of glucose metabolism to dietary modification is crucial for maintaining renal resilience under stress conditions.

During renal IRI, a sudden disruption in oxygen and nutrient supply to this metabolically active organ leads to functional decline, commonly manifested by reactive oxygen species production, release of pro-inflammatory and pro-fibrotic factors, and increased proximal tubule cell death[58]. While renal IRI enforces drastic metabolic shifts guided by signals such as nutrient availability, we propose that dietary modulation of the pre-existing metabolic state of the kidney can enhance its adaptive capacity to IRI conditions, potentially mitigating or preventing the onset of AKI[15]. With an MF diet regimen, we observed substantial protection against renal IRI. Utilizing an MRM-based LC-MS/MS method developed for in vivo isotopic tracing of glucose and fatty acid metabolism in the mouse kidney, we provided direct evidence of post-IRI metabolic activity, addressing a critical knowledge gap.

Interestingly, our data indicate that partial MR (0.17%) over 7 days failed to confer renal protection, in contrast to the robust benefit of methionine deprivation. This may reflect both insufficient intensity and limited duration of restriction, as serum methionine levels were not significantly reduced in the 0.17% group and inter-individual variability was higher, leading to a lack of statistical difference in kidney outcomes (Fig. 3d). Previous work has shown that renoprotective effects of MR often require stronger or longer interventions, such as 0.12% methionine for 12 weeks in nephrectomized mice[59] or 0.16% methionine for 15 weeks to suppress cyst growth in polycystic kidney disease[60]. These findings suggest that the renal protective efficacy of MR exhibits threshold and time dependence, and more moderate dietary restriction may require an extended duration to achieve comparable metabolic and functional benefits.

It is noteworthy that the MF diet induced significant weight loss despite unchanged caloric intake, consistent with increased energy expenditure and lipid utilization[61-63]. While weight reduction may contribute to improved ischemic tolerance through lowered leptin signaling and adipose-derived inflammation[26,64,65], our data suggest that this alone is insufficient: pharmacological inhibition of fatty-acid oxidation did not reproduce the renoprotective phenotype (Fig. 4n-r). Instead, MR can engage weight-independent pathways, including FGF21 induction, and activating the transsulfuration axis thereby increasing hydrogen sulfide production, which together enhance stress resistance and limit tissue injury[31,66]. These findings suggest that the protection afforded by MF feeding arises from the integration of weight-dependent and weight-independent mechanisms, with the latter likely persisting even under weight-matched conditions.

MR has been shown to confer renoprotection through diverse mechanisms, including suppression of inflammation and fibrosis in CKD[59], attenuation of cyst growth via methionine–SAM–Mettl3–m^6A signaling in ADPKD[60], and delay of kidney senescence via H_2S–AMPK signaling[67]. MR also enhances renal insulin sensitivity and upregulates renoprotective genes such as Sirt1 and FGF21[68]. Our findings extend prior work by demonstrating that MR promotes pyruvate oxidation and TCA cycle engagement following IRI, a mechanism that parallels the protective effect of PDK4 inhibition on ischemic injury[69]. It is likely that renal metabolic rewiring as a unifying feature of MR, positioning enhanced glucose oxidation as a central node of its acute protective effect.

Can SGLT2 inhibitors, which are commonly recommended for chronic kidney disease, induce metabolic effects similar to those observed with MR diets? SGLT2 inhibitors block glucose reuptake in the proximal tubule, leading to increased urinary glucose excretion and reduced intracellular glucose availability in renal tubular cells[70]. Under these conditions, glycolytic flux is likely diminished due to limited substrate supply, which reminiscent of caloric restriction[71,72]. To sustain energy production, renal metabolism consequently shifts toward enhanced fatty acid oxidation and ketone body utilization as alternative fuels[73-75]. Through this metabolic reprogramming, SGLT2 inhibition transforms kidney metabolism from a high-glucose, energy-intensive, and hypoxia-prone state into a more oxidative, energy-efficient, and stress-resistant profile. In contrast, our study suggests that the MF diet promotes a coordinated acceleration of both glucose and fatty acid oxidation in the context of sufficient systemic glucose availability. This difference in metabolic starting points and resultant flux patterns indicates that the MF diet and SGLT2 inhibitors likely confer protection through different metabolic adaptations.

A key question that arises is why MR-directed reprogramming of glucose metabolism is crucial for resisting renal IRI. Addressing this is complex, given the diverse roles of methionine and its related metabolites in modulating cellular activities such as gene expression[76], autophagy[77], and translation[78], and immune responses including inflammation[79]. However, from a metabolic perspective, methionine scarcity may precondition the kidney by adjusting metabolic processes necessary for adaptation or transition during IRI. Emerging evidence from cellular studies indicates that the protective effects of MR can rely on mitochondrial lipoylation, a lipid modification essential for operating the TCA cycle[80,81] and directly linked to glucose metabolism[82]. These mechanisms likely underlie the renal protection observed with the MF diet, which warrants further investigation.

In the IRI setting, impaired renal excretion renders even modest intravenous injection volumes hazardous: positive balance rapidly raises venous and interstitial pressures, reduces the transrenal pressure gradient, and promotes kidney and other organ congestion[56,83]. Consistent with this physiology, clinical AKI cohorts show that fluid accumulation independently associates with higher mortality and poorer renal recovery[84]. Moreover, AKI induces inflammatory and permeability changes in distant organs (notably lung)[85], lowering the threshold for decompensation with superimposed fluid[86]. These considerations support our interpretation that the abrupt deaths observed in control-diet IRI mice during [U-$^{13}C_6$] glucose infusion most likely reflect lethal volume loading in an AKI-sensitized milieu, while we acknowledge contributions from reduced metabolic reserve, hemodynamic and oxygen-handling vulnerabilities.

In summary, the implications of our findings extend beyond basic research, suggesting potential dietary interventions for clinical management of AKI. By leveraging MR as a metabolic strategy, we could potentially improve patient outcomes in AKI scenarios, particularly in elective surgeries that involve transient blood flow limitation, such as organ transplantation and cardiovascular procedures. Moreover, our insights into the modulation of glucose metabolism may inform therapeutic approaches aimed at enhancing renal resilience through dietary modifications or targeted pharmacological interventions. Future studies should explore the applicability of these findings in human cohorts, paving the way for novel dietary guidelines and treatment protocols that prioritize metabolic health in the context of kidney disease.

Figure legends

Fig. 1: Multi-omics analyses reveal systemic changes in kidney metabolism in response to renal IRI

a) Schematic illustrating the renal IRI surgery procedure and left kidney collection from sham and IRI groups.

b) Multi-omics profiling of kidney responses to renal IRI, with increased (red) and decreased (blue) analytes in IRI kidneys.

c-d) GO biological process terms for upregulated (red) and downregulated (blue) analytes in IRI kidneys based on transcriptomics (c) and proteomics (d).

e) KEGG pathway analysis of upregulated (red) and downregulated (blue) metabolites in IRI kidneys.

f) GSEA of the transcriptome comparing gene signatures between IRI and sham kidneys. The hash plot beneath the GSEA curve shows individual gene ranks. Left-leaning curves (positive enrichment score) indicate higher pathway expression in the IRI group, while right-leaning curves (negative enrichment score) indicate lower expression in the sham group. Normalized enrichment score (NES) and nominal p-value are indicated in order by term name.

g) Joint pathway annotation of IRI-associated molecules from the three omics datasets using OmicsNet. Colors denote molecule types: gray for RNA, red for protein, and yellow for metabolite. Node size reflects betweenness, indicating the number of direct connections to other nodes, while edges represent direct connections from existing databases. The top 20 nodes with the highest betweenness are labeled. KEGG pathway analysis revealed significant enrichment in pathways related to lipid metabolism, amino acid metabolism, and glucose metabolism.

h) Relative abundances of methionine-related metabolites in the kidney of sham and IRI groups (n = 5 per group).

All data are represented as mean ± SD, with individual points showing the n of each group. Statistical significance was assessed using unpaired two-sided Student's t-tests, with significance indicated as follows: *$p < 0.05$, **$p < 0.01$, ***$p < 0.001$. Figure a was created with BioRender.com.

Fig. 2: The kidney is a SAM-consuming organ

a) Relative abundances of methionine-related metabolites in the serum of sham and IRI groups (n = 5 per group).

b) Relative abundances of methionine-related metabolites in the serum of vehicle (n = 6) and cisplatin-induced AKI groups (n = 8).

c) Relative abundances of methionine-related metabolites in the serum of control (n=32) and SA-AKI patients (n = 18).

d) Relative abundances of methionine-related metabolites in the serum of control (n = 36) and CSA-AKI patients (n = 34).

e) Schematic of the PEMT-mediated conversion of phosphatidylethanolamine (PE) to phosphatidylcholine (PC) as a major SAM-consuming reaction (top). Western blot analysis of liver tissues from WT and global *Pemt* knockout (*Pemt* $^{-/-}$) mice (bottom).

f) Relative serum SAM levels in WT sham, WT IRI, *Pemt* $^{-/-}$ sham, and *Pemt* $^{-/-}$ IRI groups (n = 5 mice per group).

g-h) BUN (g) and sCr (h) levels in WT sham, WT IRI, *Pemt*$^{-/-}$ sham, and *Pemt*$^{-/-}$ IRI groups (n = 5 per group).

i) Experimental timeline of SAM (10 mg/kg) or PBS intraperitoneal injections during a 7-day CD diet, followed by IRI or sham surgery.

j) Serum SAM levels measured 30 min after injection by LC–MS (n = 5 mice per group).

k-l) Renal function 24 h post-surgery: BUN (k) and sCr (l) in PBS- and SAM-treated IRI mice (n = 3 in PBS sham group, n = 4 in PBS IRI group, n = 3 in SAM sham group, and n = 4 in SAM IRI group).

m) Experimental schema of sham or IRI (30-min ischemia followed by 30- or 120-min reperfusion) with left kidney and serum collection (n = 4 per group).

n) Early time-course of serum SAM levels after kidney IRI (n = 4 per group).

o-p) Positive correlations between serum SAM and BUN (o) or sCr (p) in IRI mice (red) and sham mice (grey). Data represent individual mice (n = 4 per group). Shaded areas indicate 95% confidence intervals.

All data are represented as mean ± SD, with individual points representing the sample size (n) for each group. Statistical significance was assessed using unpaired two-sided Student's t-tests (a-d, f-h, and j-l), or one-way ANOVA with a multiple comparison adjustment using Tukey's method (n) with significance noted as follows: *p < 0.05, **p < 0.01, ***p < 0.001. For panels o–p, simple linear regression was performed.

Fig. 3: Dietary methionine deprivation enhances renal resilience against IRI

a) Schematic of the 7-day dietary regimen prior to kidney IRI surgery.

b) Body weight of mice over the 7-day period on control (CD), methionine restriction (MR), and methionine-free diets (MF) (n = 9 per group).

c) Average daily caloric intake of mice over 7 days on the respective diets, calculated from daily food consumption (n = 9 per group).

d) Relative serum methionine levels in mice after the 7-day dietary regiment (n=6 per group) in a separate experiment where serum was collected for metabolite analysis without surgery.

e-f) BUN (e) and sCr (f) levels post-surgery across four groups: control diet sham (CD Sham), control diet IRI (CD IRI), methionine-free diet sham (MF Sham), and methionine-free diet IRI (MF IRI) groups (n = 8 per group).

g-h) Relative abundance of SAM levels in kidney tissue (g) and serum (h) post-surgery, measured in CD Sham (n = 4), CD IRI (n = 6), MF Sham (n = 4), and MF (n = 6) IRI groups.

i) Representative H&E stained kidney sections from CD Sham, CD IRI, MF Sham, and MF IRI groups. Scale bar: 20 μm.

j) Quantification of kidney injury based on H&E staining (n = 5 per group).

k) Representative images of renal LCN2 immunohistochemical staining in kidney sections from CD Sham, CD IRI, MF Sham, and MF IRI groups. Scale bar: 20 μm.

l) Quantification of LCN2-positive area intensity (n = 5 per group).

m) Western blot analysis of LCN2 and KIM1 protein levels in kidney tissue from CD Sham, CD IRI, MF Sham, and MF IRI groups (n = 3 per group).

n-o) Serum levels of ALT (n) and AST (o) from CD Sham, CD IRI, MF Sham, and MF IRI groups (n = 8 per group).

All data are represented as mean ± SD, with the sample size (n) for each group shown as individual points. Statistical significance was assessed using one-way ANOVA with a multiple comparison adjustment using Tukey's method (b) or unpaired two-sided Student's t-tests (c-h, j, l, and n-o), with significance noted as follows: *$p < 0.05$, **$p < 0.01$, ***$p < 0.001$. ‘ns’ denotes no significance.

Fig. 4. MF diet enhances FAO activity in kidneys

a) Schematic illustrating the metabolic changes in TECs in response to injury. Abbreviations: FAO, fatty acid β-oxidation; Glu, glucose; AcCoA, acetyl-CoA; Pyr, pyruvate; Cit, citrate; αkg, α-ketoglutarate; Suc, succinate; Fum, fumarate; Mal, malate; Oxa, oxaloacetate.

b) Representative images of renal Oil Red O staining in CD Sham, CD IRI, MF Sham, and MF IRI groups. Scale bar: 30 μm.

c) Quantification of Oil Red O staining in kidneys (n=5 per group).

d) Volcano plot showing differential analysis of renal lipidomics in kidney tissues from CD IRI and CD Sham groups.

e) Quantification of renal TAG in CD IRI, CD Sham, MF Sham, and MF IRI groups (n = 5 per group).

f) Log_2 fold-change (FC) of individual TAG species in kidneys from CD IRI vs. CD Sham and MF Sham vs. MF IRI groups.

g) Representative transmission electron microscopy (TEM) images of kidney tissue sections from CD IRI, CD Sham, MF Sham, and MF IRI groups. “N” indicates the nucleus; red circles indicate LDs. Scale bar: 2 μm.

h) Quantification of the number and area of LDs per TEC from TEM images (n = 10 per group).

i) Schematic of [^{13}C16]-palmitate stable isotope injection in mice after a 7-day dietary intervention with either a CD or MF diet. Figure created with BioRender.com.

j) Diagram illustrating palmitate metabolism and metabolites derived from [^{13}C16]-palmitate. Abbreviations: PCoA, palmitoyl CoA; Pcarnitine, palmitoylcarnitine; FAO, fatty acid β-oxidation; AcCoA, acetyl-CoA; TCA, tricarboxylic acid cycle; αkg, α-ketoglutarate; Fum, fumarate; Mal, malate.

k-m) Fractional enrichment (%) of ^{13}C-labeled metabolites from [^{13}C16]-palmitate in CD and MF groups (n = 8 per group).

n) Schematic of the FAO pathway, highlighting the specific inhibition step of CPT1 by the inhibitor etomoxir.

o) Schematic showing etomoxir (Eto) or PBS injection (Veh), followed by a 7-day MF diet and IRI surgery.

p) Renal TAG levels in Veh and Eto groups following IRI surgery and a 7-day MF diet, measured by mass spectrometry (n = 5 per group).

q-r) BUN (q) and sCr (r) levels in Veh and Eto groups after IRI surgery following a 7-day MF diet (n = 5 per group).

All data are represented as mean ± SD, with the sample size (n) for each group shown as individual points. Statistical significance was assessed using unpaired two-sided Student's t-tests (c-e, h, k-m, and p-r). Significance levels: *$p < 0.05$, **$p < 0.01$, ***$p < 0.001$. 'ns' denotes no significance.

Fig. 5: IRI and MF diet enhance glucose utilization in mouse kidneys

a) Schematic showing the experimental process of [$^{13}C6$]-glucose infusion in mice following a 7-day dietary intervention and subsequent kidney surgery. Figure created with BioRender.com.

b) Survival curves during the 150-minute [$^{13}C6$]-glucose infusion (n=5 for CD Sham, n=10 for CD IRI, n=8 for MF Sham, and n=7 for MF IRI). Note that only the surviving mice from the CD IRI group (n=5) after the 150-minute infusion were used for metabolite analysis.

c-d) Relative abundance of serum glucose labeled with six carbons (m+6) (c) and non-labeled serum glucose (m+0) (d) in CD Sham (n = 5), CD IRI (n = 5), MF Sham (n = 8), and MF IRI groups (n = 7). Each data point reflects blood collected from different mice.

e) Fractional levels of unlabeled serum glucose (m+0) in CD Sham (n = 5), CD IRI (n = 5), MF Sham (n = 8), and MF IRI groups (n = 7).

f) LC-MS analysis of glucose spectral peak areas in various labeled forms in kidney tissue from CD Sham (n = 5), CD IRI (n = 5), MF Sham (n = 8), and MF IRI (n = 7) groups. Black and purple asterisks denote statistical significance for the total (sum of labeled and unlabeled) glucose and specifically m+6 glucose, respectively.

g) Fractional levels of renal glucose (m+0) in CD Sham (n = 5), CD IRI (n = 5), MF Sham (n = 8), and MF IRI groups (n = 7).

All data are represented as mean ± SD, with the sample size (n) for each group shown as individual points. Statistical significance was assessed using Mantel-Cox test for survival analysis (b), unpaired two-sided Student's t-tests (c-e, g) or two-way ANOVA with Tukey's multiple comparisons test (f). Significance is indicated as: *p < 0.05, **p < 0.01, ***p < 0.001. 'ns' denotes no significant difference.

Fig. 6: The complete oxidation of glucose via the TCA cycle is impaired under IRI but effectively restored by the MF diet

a) Schematic representation of the glycolytic flux of [U-^{13}C]-glucose to pyruvate (m+3) and lactate (m+3).

b-c) Fractional enrichment (%) of lactate (m+3) (b) and pyruvate (m+3) (c) in the kidney following [U-^{13}C]-glucose infusion in CD Sham (n = 5), CD IRI (n = 5), MF Sham (n = 8), and MF IRI (n = 7) groups.

d) Ratio of lactate (m+3) to pyruvate (m+3) in the kidneys of mice infused with [U-^{13}C]-glucose in CD Sham (n = 5), CD IRI (n = 5), MF Sham (n = 8), and MF IRI (n = 7) groups.

e) Schematic showing [U-^{13}C]-glucose metabolism into acetyl-CoA, its entry into the TCA cycle, and subsequent conversion from αKG to glutamate via cataplerosis. αKG, α-ketoglutarate.

f-h) Fractional enrichment (%) of acetyl-CoA (m+2) (f), fumarate (m+2) (g), and malate (m+2) (h) in the kidneys following [U-^{13}C]-glucose infusion in CD Sham (n = 5), CD IRI (n = 5), MF Sham (n = 8), and MF IRI (n = 7) groups.

i) Illustration of ^{13}C labeling from [U-^{13}C]-glucose through two turns of the TCA cycle. αKG, α-ketoglutarate; glu, glutamate; gln, glutamine; mal, malate.

j-l) Fractional enrichment (%) of glutamate (m+3) (j), glutamine (m+3) (k), and malate (m+3) (l) in the kidneys following [U-^{13}C]-glucose infusion in CD Sham (n = 5), CD IRI (n = 5), MF Sham (n = 8), and MF IRI (n = 7) groups.

All data are represented as mean ± SD, with the sample size (n) for each group shown as individual points. Statistical significance was assessed using unpaired two-sided Student's t-tests. Significance is indicated as: *$p < 0.05$, **$p < 0.01$, ***$p < 0.001$.

Fig. 7: Chemical activation of pyruvate oxidation is sufficient to exert renal protection against IRI

a) Schematic illustrating the pathways of glycolysis, lactate fermentation, the TCA cycle, and cataplerosis, highlighting key enzymes involved in these metabolic processes. Abbreviations: G6P, glucose-6-phosphate; F6P, fructose-6-phosphate; FBP, fructose-1,6-bisphosphate; GAP, glyceraldehyde-3-phosphate; DHAP, dihydroxyacetone phosphate; 1,3BPG, 1,3-bisphosphoglycerate; 3PG, 3-phosphoglycerate; 2PG, 2-phosphoglycerate; PEP, phosphoenolpyruvate; PYR, pyruvate; Lac, lactate; ACCoA, acetyl-CoA; OAA, oxaloacetate; CIT, citrate; cisA, cis-aconitate; ICIT, isocitrate; αKG, α-ketoglutarate; SUCC, succinate; FUM, fumarate; MAL, malate; GLU, glutamate; GLN, glutamine.

b) Heatmap displaying the levels of enzymes involved in glycolysis and the TCA cycle in the kidneys from CD Sham, CD IRI, MF Sham, and MF IRI groups (n = 3 mice per group).

c) Schematic depicting the action mechanism by which the PDK inhibitor DCA activates PDH.

d) Schematic illustrating the experimental design of 7-day DCA treatment through drinking water, followed by kidney IRI surgery.

e-f) BUN (e) and sCr (f) levels following renal IRI surgery in control diet (CD) plus vehicle, control diet (CD) plus DCA, and MF diet plus DCA groups (n = 5 mice per group).

g) Representative images of renal H&E staining from indicated groups. Scale bar: 20 μm.

h) Quantification of the renal H&E staining in the indicated groups (n = 5 per group).

All data are represented as mean ± SD, with the sample size (n) for each group shown as individual points. Statistical significance was assessed using unpaired two-sided Student's t-tests. Significance is indicated as: *p < 0.05, **p < 0.01, ***p < 0.001. 'ns' denotes no significant difference.

Methods

Mice husbandry

All procedures and animal husbandry followed the National Institutes of Health Guide for the Care and Use of Animals and were approved by the Ethics Committee of Zhejiang University under project license ZJU20240264. We have complied with all relevant ethical regulations for animal use. Due to the significant difference in susceptibility to IRI between male and female mice, only male mice were used to minimize the total number required for statistical analysis[87]. Six-week-old male C57BL/6 mice were purchased from SLAC Laboratory Animal Company (Shanghai, China) and were adaptively fed for 1 week and provided with free access to a standard chow diet (SLAC, P1101F) and drinking water before entering studies. The mice were acclimatized and maintained under specific pathogen-free conditions at the Experimental Animal Center of Zhejiang University. They were housed in ventilated cages with a 12-hour light-dark cycle, at approximately 22°C temperature with 55 ± 10% humidity and had ad libitum access to food and water.

Generation of global *Pemt* knockout mice

Pemt $^{flox/+}$ (*Pemt* $^{fl/+}$) mice (C57BL/6J) were generated through standard homologous recombination at the Shanghai Model Organisms Center (Shanghai, China), with *Pemt* exon 3 flanked by *loxP* sequences. These floxed *Pemt* mice were backcrossed with C57BL/6J mice to establish a congenic strain. Subsequently, *Pemt* $^{fl/+}$ mice were mated with Dppa3-IRES-Cre mice (C57BL/6J) from the same center. The IRES-Cre was inserted into the 3'UTR of the Dppa3 gene, which is expressed in primordial germ cells and during early embryonic development. This enabled Cre recombinase activity in early embryos and germ cells, triggering homologous recombination between *loxP* sites, leading to the deletion of exon 3 in all cells of the developing animal, including germ cells that transmit the genetic modification to offspring.

The deletion of exon 3 disrupts the signal peptide and open reading frame, resulting in loss of *Pemt* expression. Due to potential mosaic activity from Cre recombinase activity, the first generation of Dppa3-IRES-Cre *Pemt* $^{fl/+}$ mice might be chimeric. Chimeric offspring were backcrossed to C57BL/6J to produce *Pemt* $^{+/-}$ mice, which were then interbred to generate *Pemt* $^{-/-}$ mice. Genomic DNA from mouse tails was extracted for genotyping by PCR using the following primers: 5'-CCAGCAGGGCAATCCTAACA-3' and 5'-AGGGCAAGACAGGAACGAAG-3'. PCR products of 1422 bp, 1533 bp, and 784 bp correspond to wild-type, floxed without Cre activity, and floxed with Cre activity (null alleles), respectively.

IRI-induced AKI models

Mice were anesthetized using 1.5% isoflurane gas and placed on a 37°C warming pad. The abdomen was opened, and the right kidney was surgically removed simultaneously with the induction of left kidney ischemia, which was achieved by applying a nontraumatic micro titanium clip to the left renal pedicle for 30 minutes. The sham group underwent the same procedure, except for kidney removal and clamping. During surgery, all mice received 0.5 ml intraperitoneal warm sterile saline to prevent dehydration. The mice were kept on the warming pad until they fully regained consciousness before being returned to their cages. Kidney and blood samples were collected 24 hours after IRI surgery. For exogenous SAM administration in IRI, mice were maintained on control diet for 7 days and received intraperitoneal injections of S-adenosyl-L-methionine (SAM; 10 mg kg^{-1} in sterile PBS) (Sangon, A351020) or an equal volume of PBS on day 7 and again on day 8 (the day of IRI)[88]. Thirty minutes after each injection, blood was collected from the tail vein for serum metabolite measurements (see the Metabolomics section for detailed procedures). Renal IRI surgery, perioperative care and sample collection was performed as described above.

Cisplatin-induced AKI models

Mice were injected intraperitoneally with a single dose of cisplatin (20 mg/kg BW) (Selleck, S1166) dissolved in normal saline. Equivalent dose of saline water was used for the vehicle group. Kidney and blood samples were collected 72 hours after cisplatin treatment.

Diet modifications

Before the experiment began, mice were randomly assigned to receive one of the following diets: 0.86% methionine (control diet, M20121704), 0.17% methionine (methionine restriction, M22121202), or 0% methionine (methionine free, M11709). All diets were obtained from Moldiets and irradiated. In these diets, calories from amino acids were replaced by calories from carbohydrates, while calories from fat were kept constant at 11.6%, making the diets isocaloric (3.872 kcal g^{-1}). Detailed composition of the diets were provided in Supplementary Data 1.

DCA administration

Mice were randomly divided into two groups and administered either sodium dichloroacetate (DCA) (Sigma-Aldrich, 347795) or sodium chloride (Sangon, A501218-0005) dissolved in drinking water. Based on an average daily water intake of approximately 5 mL per adult mouse, 500 mg/L of DCA (3.3 mM) or an equimolar concentration of NaCl was added to the drinking water[89]. After

7 days of treatment with DCA or sodium chloride in the drinking water, mice underwent renal IRI surgery, with details as previously described.

Etomoxir administration

Mice were randomly divided into the etomoxir group and the control group. Etomoxir (MCE, HY-50202A) was administered intraperitoneally 20 mg/kg dose 24 hours before and on the day of IRI surgery. The control group received an equivalent dose of phosphate buffered saline (Sangon, B548117-0500). Mice in the etomoxir group and the control group underwent renal IRI surgery, as detailed previously.

Stable-isotope labeling in vivo

The infusion rate and duration were based on previous studies [50,51]. For the [U-^{13}C6]-glucose infusion, mice were subjected to either IRI or sham surgery under their respective dietary conditions, with the reperfusion time precisely recorded to the minute. The infusion lasted for 2.5 hours unless otherwise noted. To track metabolism at the time point of 24-hour post-reperfusion, infusion began at 21.5 hours post-reperfusion (24h minus 2.5h). Mice were infused with 300 mM [U-^{13}C6]-glucose (Cambridge Isotope Laboratories, CLM-1396-10) dissolved in normal saline. The mice were anesthetized with isoflurane and received the infusion intravenously (iv) via the tail vein. The infusion rate was set to 0.1 μL min^{-1} g^{-1}. The mice were closely monitored for survival throughout the infusion, and observations were recorded. The experiment endpoint was defined as either the completion of the infusion or the death of the mouse.

For the [U-^{13}C16]-palmitic acid infusion,4mM [U-^{13}C16]-palmitic acid was conjugated with fatty acid-free bovine serum albumin (Sangon, A602448-0050) at a PA:BSA molar ratio of 4:1. Mice were anesthetized with isoflurane and injected intravenously (iv) into the tail vein. The infusion rate was set to 0.4 μL min^{-1} g^{-1} and lasted for 2.5 hours. Upon completion of the infusion, the kidneys and blood of the mice were collected.

Euthanasia and collection of tissues

At the end of the experiment, mice were anesthetized with isoflurane in accordance with approved protocols. Blood was collected via retro-orbital sinus puncture, followed by euthanasia by cervical dislocation under deep isoflurane anesthesia. Tissues (kidney and liver) were quickly harvested (< 2 min). The kidneys were sharply bisected into four equal parts on ice. The middle two portions were fixed in 4% paraformaldehyde (Sangon, E672002-0500) for paraffin and cryo-embedding, respectively, while the remaining two portions were flash-frozen in liquid nitrogen and stored at -80°C until further analysis.

Patients sample

Serum samples from all patients were collected from the intensive care unit (ICU) of the First Affiliated Hospital, Zhejiang University School of Medicine. The study was conducted in accordance with the principles of the Declaration of Helsinki and was approved by the Research Ethics Committee of the First Affiliated Hospital, Zhejiang University School of Medicine (IIT20241041) following the acquisition of informed consent from all participants. All ethical regulations relevant to human research participants were followed. All serum samples diagnosed with AKI were classified according to the KDIGO Clinical Practice Guideline definition of AKI[90]. The detailed information about the patients is shown in Supplementary Data 1.

For the sepsis patient cohort, sepsis was diagnosed based on The Third International Consensus Definitions for Sepsis and Septic Shock[91], and patients' detailed diagnoses were further assessed by clinicians. Blood samples were collected upon admission, and based on blood samples taken 48 hours post-admission, patients were diagnosed with sepsis-associated AKI (SA-AKI) or without AKI. Patients younger than 18 years of age, or those with chronic kidney disease (CKD), a history of kidney transplantation, pregnancy, or a prior history of AKI were excluded.

For the cohort of patients undergoing cardiac surgery, blood samples were collected upon admission, and based on blood samples taken 48 hours after cardiopulmonary bypass (CPB) cardiac surgery, patients were diagnosed with cardiac surgery-associated AKI (CSA-AKI) or without AKI. Patients under 18 years of age, or patients with a history of kidney transplantation, recent urinary tract infections or obstruction, pregnancy, or a prior history of AKI were excluded.

Renal and liver function

Blood was collected into sterile tubes and left undisturbed to clot for 30 minutes at room temperature. The samples were then centrifuged at 4°C, 1000g for 10 minutes to obtain serum. A 10 μL aliquot of the serum was analyzed using a dry chemistry analyzer (Fujifilm 7000i) with the corresponding slides to measure renal function indicators, including BUN and sCr, as well as liver function indicators, ALT and AST, following the manufacturer's instructions.

Transcriptomic analysis

Total RNA was isolated from mouse kidneys using TRIzol reagent (Invitrogen) following the manufacturer's protocol. After confirming RNA quality, libraries were constructed using the Illumina TruSeq RNA Preparation Kit. Sequencing was performed on Illumina HiSeq platforms with a 2×150 paired-end configuration at the Genewiz Core Facility. Low-quality sequences, including adapters and bases with a quality score below 20, were trimmed using Cutadapt (v1.9.1). Clean reads were aligned to the mouse reference genome (GRCm38) using Hisat2 (v2.0.1). Gene and isoform expression levels were quantified using HTSeq (v0.6.1). Differential expression analysis was performed using the DESeq2 Bioconductor package.

Proteomics analysis

Mouse kidneys were ground in a pre-cooled mortar with liquid nitrogen and lysed in 4 volumes of lysis buffer (8 M urea, Sigma-Aldrich, 1% protease inhibitor, Merck Millipore) followed by sonication. After centrifugation, protein concentration in the supernatant was determined using a BCA protein assay kit. Equal amounts of protein were digested overnight with trypsin (Promega). Dithiothreitol (DTT) was added to a final concentration of 5 mM and incubated at 56°C for 30 minutes for reduction. Iodoacetamide (IAA) was then added to a final concentration of 11 mM and incubated at room temperature in the dark for 15 minutes for alkylation. Peptides were dissolved in mobile phase A and separated using an Easy-nLC1000 ultraperformance liquid chromatography system. Mobile phase A consisted of water with 0.1% formic acid and 2% acetonitrile; mobile phase B consisted of acetonitrile with 0.1% formic acid. The gradient was set as follows: 0-14 minutes, 6%-24% B; 14-16 minutes, 24%-35% B; 16-18 minutes, 35%-90% B; 18-20 minutes, 90% B. The flow rate was maintained at 500 nl/min. After separation, peptides were ionized via a capillary ion source and analyzed using a timsTOF Pro mass spectrometer. The ion source voltage was set to 1.75 kV, and both precursor ions and their fragments were detected and analyzed by time-of-flight (TOF). Data were acquired in data-independent acquisition-parallel accumulation serial fragmentation (dia-PASEF) mode. The primary MS scan range was set to 300-1500 m/z, followed by 20 PASEF scans. The MS/MS scan range was 400-850 m/z, with a window size of 7 m/z.

The DIA data were analyzed using the DIA-NN search engine (v.1.8). Tandem mass spectra were searched against a concatenated database of Mus_musculus_10090_SP_20230103.fasta (17,132 entries) and a reverse decoy database. Trypsin/P was designated as the cleavage enzyme, allowing for up to one missed cleavage. N-terminal methionine excision and carbamidomethylation on cysteine were specified as fixed modifications. The false discovery rate (FDR) was adjusted to < 1%. Proteomics analysis was conducted by PTM Biolabs (Hangzhou, China).

Metabolomics

For tissue metabolite extraction, 5 mg of fresh frozen tissue was mixed with 400 µL of 60% methanol (A456-4, Thermo Fisher) and an equal volume of glass beads (Z250465, Sigma). The samples were homogenized using an automatic sample grinder (JXFSTPRP, Jingxin). After centrifugation at 4,000g for 2 minutes at 4°C, the samples were washed with 200 µL of the same buffer and centrifuged again at 4,000g for 2 minutes at 4°C. The supernatant was collected and centrifuged at 15,000g for 10 minutes at 4°C. A total of 500 µL of the supernatant was transferred to a new tube and centrifuged again at 15,000g for 10 minutes at 4°C. A final volume of 450 µL was transferred to a new tube, and solvents were evaporated to dryness using a vacuum concentrator and stored at −80°C until analysis.

For serum metabolite extraction, 5 µL of serum was mixed with 200 µL of 60% methanol (A456-4, Thermo Fisher) and homogenized using the automatic sample grinder (JXFSTPRP, Jingxin). The samples were centrifuged at 15,000g for 10 minutes at 4°C, and the supernatant was collected. Solvents were evaporated to dryness using a vacuum concentrator (Labconco) and stored at −80°C until analysis.

For metabolite preparation, each polar dry pellet was redissolved in 150 µL of 60% acetonitrile (AC610010040, Sigma) with 1/50 volume of amino acid standards mix set A (NSK-A, Cambridge Isotope Laboratories). Metabolites were quantified using LC-MS/MS with a triple quadrupole mass spectrometer (QTRAP 6500+ System; AB SCIEX) following previously established methods[92,93]. In brief, the redissolved metabolites were chromatographically separated using a SeQuant Zichydrophilic interaction liquid chromatography (pHILIC) column (5 µm polymer, 150 × 2.1 mm; MilliporeSigma). Separation was performed on a high-performance LC system (ExionLC AD System) coupled to a triple quadrupole mass spectrometer (QTRAP 6500+ System; AB SCIEX). A 34-minute liquid chromatography was conducted on the pHILIC column at a flow rate of 0.15 mL/min, using 20 mM ammonium carbonate with 0.1% ammonium hydroxide as solvent A, and 100% acetonitrile as solvent B. The gradient elution was as follows: 80% solvent B at 0.01 min, 20% solvent B at 20 min, 80% solvent B at 20.5 min, and held at 80% solvent B until 34 min. Metabolites were detected using MRM transitions in both positive and negative ion modes. The retention time of each MRM peak was matched to the corresponding standard, and the peak area was quantified using Analyst Software (v2.0). Absolute quantification of methionine in each sample was performed by calculating its concentration based on the target concentrations of the amino acid standards mix set A and the volumes used during the procedure.

Pathway enrichment analysis

For identifying differentially expressed genes in RNA-seq analysis, DESeq2 (v1.26.0) from the Bioconductor package was used to perform differential expression analysis based on read count data. Genes were considered significantly different if they had a fold change (FC) of ≥2 and an p-value of <0.05. For identifying differentially expressed protein in proteomics analysis, following the DIA-NN (v1.8) database search, normalized intensity values (corrected intensity across samples) were used to calculate relative protein abundance. A two-tailed unpaired t-test was conducted on relative abundances between groups to identify differentially expressed proteins with FC ≥ 1.5 and p-value <0.05. For identifying differentially expressed metabolites in metabolomics, Analyst Software OS v2.0 was used to quantify peak areas, and a two-tailed unpaired t-test was applied to detect differentially expressed metabolites, defined as those with p-value <0.05 between the two groups.

Differentially expressed genes and proteins were analyzed using the Metascape web tool[94] for Gene Ontology (GO) analysis, following the prompts provided on the platform. KEGG pathway analysis of differentially expressed metabolites was conducted using MetaboAnalyst (v6.0)[95]. Gene Set Enrichment Analysis (GSEA) was conducted using the clusterProfiler R package (v4.10.0)[96] to evaluate the enrichment of gene sets of interest, following the provided guidelines. The pathways of interest were obtained from the Mouse Molecular Signatures Database (MSigDB), including hallmark gene sets (hypoxia #MM3861, inflammatory response #MM3890, apoptosis #MM3869, and oxidative phosphorylation #MM3893), Gene ontology biological process (fatty acid β-oxidation #MM4792), and the Reactome pathway (TCA cycle #MM15407).

Joint multi-omics analysis

Integrative network analysis of the three omics layers (transcriptomics, proteomics, and metabolomics) was performed using the OmicsNetR R package (v1.0.0)[97]. Briefly, a list containing the IDs and fold changes of differentially expressed transcripts, proteins, and metabolites from each omics layer was input to construct a comprehensive network encompassing all potential interactions among the three omics. This network was visualized in 2D, resulting in a combined analysis network diagram, followed by integrative KEGG analysis of all nodes.

Weight, food and water intake measurements

The day when the mice were switched to the new diet regimens was designated as day 0. Mice were housed 2-3 per cage. Body weights were recorded on day 0, day 3, and day 7. Food intake and water consumption were calculated based on the change in weight of food and water in the cages between measurements. Daily caloric intake was calculated based on the food recipe (provided in Supplementary Data 1).

In vivo metabolic flux analysis

Blood and tissues from mice infused with different isotope-labeled solutions were collected at the indicated time points, and metabolites were extracted as described above. ^{13}C-labeled metabolites were detected using LC-MS/MS, targeting specific parent and daughter ions corresponding to the ^{13}C-labeled forms.

For isotopologue analysis, peak areas were corrected using the IsoCorrectoR R package (v1.21.0)[98] to remove the contribution of the naturally occurring isotopes and tracer purity. For a given metabolite containing *i* carbon atoms, the fractional enrichment of individual isotopologs, $F(m+x)$, was calculated by the percentage of the metabolite pool containing x ^{13}C atoms, after correcting for natural isotope correction using the following foluma:

$$F(m+x) = \frac{C(m+x)}{\sum C(m+0) + C(m+1) + \cdots + C(m+i)} \times 100\% \qquad (equation\ 1)$$

Here, i represents the number of carbon atoms in the metabolite, and $C(m+x)$ refers to the corrected peak area for the metabolite containing x ^{13}C atoms[99].

Western blotting

Mouse kidneys were lysed in in RIPA buffer (Beyotime, P0013B) supplemented with protease and phosphatase inhibitors (Beyotime, P1050 and P1051) and homogenized by bead-beating, followed by boiling at 75°C for 10 minutes. Equal amounts of protein were separated by SDS-PAGE and transferred onto polyvinylidene difluoride (PVDF) membranes. After blocking with 5% milk for 1 hour, membranes were incubated overnight at 4°C with the following primary antibodies: KIM1 (R&D, AF1817, 1:1000), LCN2 (Abcam, ab216462, 1:2000), and β-Actin (Abclonal, AC026, 1:5000). The membranes were then incubated for 2 hours at room temperature with the corresponding horseradish peroxidase-conjugated secondary antibodies, either anti-rabbit (CST, #7074, 1:5000) or anti-goat (Abcam, ab97110, 1:5000). Protein signals were detected using the Super ECL Chemiluminescence Kit (Vazyme, E411). All antibodies were commercially sourced and validated. Uncropped and unprocessed blot scans are provided in the Source Data file.

Histopathology

Kidneys were harvested and fixed in 4% paraformaldehyde for 24 hours, followed by dehydration in graded ethanol, hyalinization in xylene, and embedding in paraffin. Tissue sections were cut at 3 μm and stained with hematoxylin-eosin (H&E). The stained sections were imaged using a slide scanner. For each tissue section, 10 random high-power fields were selected. Tissue damage was assessed based on the percentage of damaged tubules: no damage (score 0), <25% damage (score 1), 25%-50% damage (score 2), 50%-75% damage (score 3), and >75% damage (score 4). The criteria for tubular injury assessment included loss of brush border, tubular dilation, cast formation, and cell lysis[100]. All scoring was conducted by an operator blinded to the experimental model.

Oil red O staining

10 μm kidney frozen sections were washed three times with pre-cooled PBS. The sections were immersed in 60% isopropanol for 2 minutes, followed by staining with freshly prepared Oil Red O solution for 30 minutes at room temperature. After staining, the sections were immersed in 60% isopropanol for 1 minute, washed with PBS, and counterstained with hematoxylin for 1 minute. The sections were mounted with glycerol gelatin and imaged using a slide scanner. For each sample, 10 random high-power fields were selected, and the red-stained areas were quantified using ImageJ blindly, following previously reported methods[101].

Immunohistochemistry (IHC)

The deparaffinized kidney sections were immersed in citrate buffer (Beyotime, P0083) and subjected to antigen retrieval at 95°C for 30 minutes. Endogenous peroxidase activity was blocked using 3% H_2O_2 for 15 minutes. After blocking (Beyotime, P0102) for 1 hour, the sections were incubated overnight at 4°C with primary antibodies Lipocalin-2 (Abcam, ab216462, 1:200). Staining was completed by incubating with Goat Anti-Rabbit IgG (Abcam, ab97051, 1:500) for 2 hours at room temperature, followed by DAB staining (Beyotime, P0203) and counterstaining with hematoxylin. All immunohistochemistry images were captured using a slide scanner and quantitatively analyzed with ImageJ software.

TEM analysis

Fresh mouse kidney tissues were collected and fixed overnight at 4°C in 2.5% glutaraldehyde solution, post-fixed in 1% osmium tetroxide for 2 hours. Dehydration was performed using a graded ethanol and acetone series, and the tissues were embedded in Spurr's resin, then cured at 70°C overnight. Ultrathin sections (70 nm) were obtained using an ultramicrotome (LEICA, EM UC7). The sections were double-stained with lead citrate and uranyl acetate for 10 minutes, placed on copper grids, and observed under transmission electron microscopy (Hitachi, H-7650) at 80 kV of accelerating voltage. Regions of interest were photographed using the CCD camera (Gatan, Model 830). The number and area of lipid droplets were measured using ImageJ software.

Lipidomics

Lipids from kidney tissue were extracted using chloroform/methanol (2:1, v/v) following previously described methods[102,103]. Briefly, 5 mg of kidney tissue was collected, weighed, and resuspended in 0.5 ml LC-MS-grade methanol (A456-4, Thermo Fisher) for bead-beating lysis. The whole lysate and precipitate were transferred to a glass tube, and 2.5 ml of chloroform (650498, Sigma) along with 0.4 ml of 50 mM citric acid (A610055, Sangon) were added for phase separation. The bottom lipid phase was collected, dried using a vacuum concentrator (Labconco), and stored at −80°C until analysis. Dried lipid extracts were resuspended in LC-MS-grade isopropanol, acetonitrile, and water (2:1:1) with 17:0 PC, 17:0 PE, and 14:0 PS spike-in standards from Lipidomix (330707-1EA-014, Avanti).

The redissolved lipid samples were quantitated using LC–MS/MS with a triple quadrupole mass spectrometer (QTRAP 5500+ System; AB SCIEX). Lipid separation was achieved on a C18 column (ACQUITY UPLC BEH C18, 130 Å, 1.7 μm, 2.1 mm × 50 mm), followed by quantification through multiple reaction monitoring (MRM) in positive mode for neutral lipids like TAG, and in negative mode for phospholipids such as PE and PC. The mobile phase consisted of buffer A (33.3% methanol, 33.3% acetonitrile, 33.4% water, and 5 mM ammonium acetate) and buffer B (5 mM ammonium acetate in 100% isopropanol). The gradient elution was run as follows: T = 0 min, 20% buffer B; T = 1 min, 20% buffer B; T = 3 min, 60% buffer B; T = 13 min, 98% buffer B; T = 13.1 min, 20% buffer B; T = 16 min, 20% buffer B. Retention times for each MRM peak were compared with the appropriate standards, and peak areas were quantified using Analyst Software OS v2.0. The actual concentration of each lipid species in the samples was calculated based on the target concentrations of the Avanti mass spec internal standard lipidomix and the volume used in the experimental procedure.

Serum fatty acid quantification by GC–MS

For lipid extraction, 5 μL of serum was mixed with 100 μL of LC-MS-grade methanol (A456-4, Thermo Fisher) for bead-beating lysis. 200 μL of chloroform and 40 μL of 50 mM citric acid were added and the mixture was vortexed and homogenized, then phase-separated by centrifugation. The lower organic phase was collected, dried under vacuum, and stored at −80 °C.

For derivatization, dried extracts were resuspended in 50 μL O-methoxylamine in pyridine at 15 mg mL^{-1}, mixed, and incubated at 30 °C for a total of 60 min. 50 μL MSTFA was then added and the mixture incubated at 30 °C for a total of 30 min. Samples were clarified at 15,000g for 15 min at room temperature. Ten microlitres of supernatant from each sample was pooled to prepare a quantity control sample, and the remaining supernatant was transferred to autosampler vials.

Derivatized samples of 1 μL were analyzed on an Agilent 8890 GC–MS in electron-ionization mode at 70 eV with the source at 250 °C. Helium carrier gas was set to 1 mL min^{-1} under constant flow with a split ratio of 10:1 and an inlet temperature of 250 °C. The oven program was 60 °C for 2 min, then ramp 12 °C min^{-1} to 165 °C and hold for 2 min, then ramp 3 °C min^{-1} to 315 °C and hold for 10 min, followed by cooling to 60 °C before each injection. Spectra were acquired over m/z 30–500. Compounds were identified by NIST 17 library matching using Unknowns Analysis v12.0 and quantified by peak areas in Quantitative Analysis v12.0.

Statistics and Reproducibility

GraphPad Prism 10 and Excel were used for statistical analysis. No statistical methods were used to predetermine the sample size. Sample sizes were determined based on our prior experience with the AKI mouse model and dietary intervention studies. Details regarding sample sizes, statistical analyses, and p-values are provided in the figure panels, figure legends, and the results section. All biological replicates were performed at least three times with consistent results.

Baseline characteristics were presented as mean ± SD (standard deviation) or median (interquartile range, 25th–75th percentiles) for continuous variables, and as absolute and relative frequencies (%) for categorical variables. Comparisons were made using Student's t-test, Mann–Whitney U test, or chi-square test, depending on the type and distribution of the data.

The Violin plots are presented as follows: each point represents an individual patient sample, with a bold central line indicating the median (50th percentile), and thinner lines above and below representing the 25th and 75th percentiles, respectively.
Mantel-Cox test was used for survival analysis. Other quantitative data are presented as mean ± SD as indicated in the figure legends. An unpaired two-sided Student's t-test was used to assess significance between two groups. Statistical significance for comparisons among three groups was determined by one-way ANOVA or two-way ANOVA with Tukey's multiple comparisons test, with details provided in each figure legend. Results are considered significant when $^{*}p < 0.05$, $^{**}p < 0.01$, $^{***}p < 0.001$

Data and materials availability

All data supporting this study are available from the corresponding author upon reasonable request. All supplementary figures and all blots include size markers, with uncropped scans provided in Supplementary Information. All Supplementary Tables have been prepared in Supplementary Data 1. All numerical source data underlying the graphs in the figures have been provided as Supplementary Data 2. RNA sequencing data are available in the Gene Expression Omnibus (GEO) with the accession number GSE283374. The proteomics data from mass spectrometry are available in the ProteomeXchange Consortium through the PRIDE repository under the dataset identifier PXD058530. Metabolomics data are available in the China National Center for Bioinformation database under BioProject PRJCA033069.

References

1 Murugan, R. & Kellum, J. A. Acute kidney injury: what's the prognosis? *Nature Reviews Nephrology* **7**, 209–217 (2011). https://doi.org/10.1038/nrneph.2011.13

2 Li, Z.-L. *et al.* Renal tubular epithelial cells response to injury in acute kidney injury. *EBioMedicine* **107**, 105294 (2024). https://doi.org/10.1016/j.ebiom.2024.105294

3 Emma, F., Montini, G., Parikh, S. M. & Salviati, L. Mitochondrial dysfunction in inherited renal disease and acute kidney injury. *Nature Reviews Nephrology* **12**, 267–280 (2016). https://doi.org/10.1038/nrneph.2015.214

4 Kaushal, G. P. & Shah, S. V. Autophagy in acute kidney injury. *Kidney International* **89**, 779–791 (2016). https://doi.org/10.1016/j.kint.2015.11.021

5 Zuk, A. & Bonventre, J. V. in *Annual Review of Medicine, Vol 67* Vol. 67 293–307 (2016).

6 Sanz, A. B., Sanchez-Niño, M. D., Ramos, A. M. & Ortiz, A. Regulated cell death pathways in kidney disease. *Nature Reviews Nephrology* **19**, 281–299 (2023). https://doi.org/10.1038/s41581-023-00694-0

7 Kellum, J. A. *et al.* Acute kidney injury. *Nature Reviews Disease Primers* **7** (2021). https://doi.org/10.1038/s41572-021-00284-z

8 Hoste, E. A. J. *et al.* Epidemiology of acute kidney injury in critically ill patients: the multinational AKI-EPI study. *Intensive Care Medicine* **41**, 1411–1423 (2015). https://doi.org/10.1007/s00134-015-3934-7

9 Al-Jaghbeer, M., Dealmeida, D., Bilderback, A., Ambrosino, R. & Kellum, J. A. Clinical Decision Support for In-Hospital AKI. *Journal of the American Society of Nephrology : JASN* **29**, 654–660 (2018). https://doi.org/10.1681/ASN.2017070765

10 Ronco, C., Bellomo, R. & Kellum, J. A. Acute kidney injury. *Lancet* **394**, 1949–1964 (2019).

https://doi.org/10.1016/S0140-6736(19)32563-2
11 Scholz, H. *et al.* Kidney physiology and susceptibility to acute kidney injury: implications for renoprotection. *Nature reviews. Nephrology* (2021). https://doi.org/10.1038/s41581-021-00394-7
12 Wang, Z. *et al.* Specific metabolic rates of major organs and tissues across adulthood: evaluation by mechanistic model of resting energy expenditure. *The American Journal of Clinical Nutrition* **92**, 1369–1377 (2010). https://doi.org/10.3945/ajcn.2010.29885
13 Chevalier, R. L. The proximal tubule is the primary target of injury and progression of kidney disease: role of the glomerulotubular junction. *American Journal of Physiology. Renal Physiology* **311**, F145–F161 (2016). https://doi.org/10.1152/ajprenal.00164.2016
14 Bordoni, L. *et al.* Longitudinal tracking of acute kidney injury reveals injury propagation along the nephron. *Nature Communications* **14**, 4407 (2023). https://doi.org/10.1038/s41467-023-40037-y
15 van der Rijt, S., Leemans, J. C., Florquin, S., Houtkooper, R. H. & Tammaro, A. Immunometabolic rewiring of tubular epithelial cells in kidney disease. *Nature Reviews Nephrology* **18**, 588–603 (2022). https://doi.org/10.1038/s41581-022-00592-x
16 Bhargava, P. & Schnellmann, R. G. Mitochondrial energetics in the kidney. *Nature Reviews Nephrology* **13**, 629–646 (2017). https://doi.org/10.1038/nrneph.2017.107
17 Kang, H. M. *et al.* Defective fatty acid oxidation in renal tubular epithelial cells has a key role in kidney fibrosis development. *Nature Medicine* **21**, 37–46 (2014). https://doi.org/10.1038/nm.3762
18 Weinberg, J. M., Venkatachalam, M. A., Roeser, N. F. & Nissim, I. Mitochondrial dysfunction during hypoxia/reoxygenation and its correction by anaerobic metabolism of citric acid cycle intermediates. *Proceedings of the National Academy of Sciences of the United States of America* **97**, 2826–2831 (2000).
19 Zager, R. A., Johnson, A. C. M. & Becker, K. Renal Cortical Pyruvate Depletion during AKI. *Journal of the American Society of Nephrology* **25**, 998–1012 (2014). https://doi.org/10.1681/asn.2013070791
20 Legouis, D. *et al.* Altered proximal tubular cell glucose metabolism during acute kidney injury is associated with mortality. *Nature Metabolism* **2**, 732–743 (2020). https://doi.org/10.1038/s42255-020-0238-1
21 Zhou, H.-L. *et al.* Metabolic reprogramming by the S-nitroso-CoA reductase system protects against kidney injury. *Nature* **565**, 96–100 (2018). https://doi.org/10.1038/s41586-018-0749-z
22 Lan, R. *et al.* Mitochondrial Pathology and Glycolytic Shift during Proximal Tubule Atrophy after Ischemic AKI. *Journal of the American Society of Nephrology* **27**, 3356–3367 (2016). https://doi.org/10.1681/asn.2015020177
23 Chrysopoulou, M. & Rinschen, M. M. Metabolic Rewiring and Communication: An Integrative View of Kidney Proximal Tubule Function. *Annu Rev Physiol* **86**, 405–427 (2024). https://doi.org/10.1146/annurev-physiol-042222-024724
24 Kalantar-Zadeh, K. & Fouque, D. Nutritional Management of Chronic Kidney Disease. *The*

New England Journal of Medicine **377**, 1765–1776 (2017). https://doi.org/10.1056/NEJMra1700312
25 Johnsen, M. *et al.* The Integrated RNA Landscape of Renal Preconditioning against Ischemia-Reperfusion Injury. *Journal of the American Society of Nephrology* **31**, 716–730 (2020). https://doi.org/10.1681/asn.2019050534
26 Robertson, L. T. *et al.* Protein and Calorie Restriction Contribute Additively to Protection from Renal Ischemia Reperfusion Injury Partly via Leptin Reduction in Male Mice. *The Journal of Nutrition* **145**, 1717–1727 (2015). https://doi.org/10.3945/jn.114.199380
27 Späth, M. R. *et al.* Organ Protection by Caloric Restriction Depends on Activation of the De Novo NAD+ Synthesis Pathway. *Journal of the American Society of Nephrology* **34**, 772–792 (2023). https://doi.org/10.1681/asn.0000000000000087
28 Hoyer-Allo, K. J. R. *et al.* Caloric restriction reduces the pro-inflammatory eicosanoid 20-hydroxyeicosatetraenoic acid to protect from acute kidney injury. *Kidney International* **102**, 560–576 (2022). https://doi.org/10.1016/j.kint.2022.04.033
29 Mitchell, J. R. *et al.* Short-term dietary restriction and fasting precondition against ischemia reperfusion injury in mice. *Aging Cell* **9**, 40–53 (2010). https://doi.org/10.1111/j.1474-9726.2009.00532.x
30 Späth, M. R. *et al.* The proteome microenvironment determines the protective effect of preconditioning in cisplatin-induced acute kidney injury. *Kidney International* **95**, 333–349 (2019). https://doi.org/10.1016/j.kint.2018.08.037
31 Hine, C. *et al.* Endogenous Hydrogen Sulfide Production Is Essential for Dietary Restriction Benefits. *Cell* **160**, 132–144 (2015). https://doi.org/10.1016/j.cell.2014.11.048
32 Wang, S.-Y., Cai, G.-Y. & Chen, X.-M. Energy restriction in renal protection. *Br J Nutr* **120**, 1149–1158 (2018). https://doi.org/10.1017/S0007114518002684
33 Doke, T. *et al.* NAD+ precursor supplementation prevents mtRNA/RIG-I-dependent inflammation during kidney injury. *Nature Metabolism* **5**, 414–430 (2023). https://doi.org/10.1038/s42255-023-00761-7
34 Clark, A. J. *et al.* Hepatocyte nuclear factor 4α mediated quinolinate phosphoribosylltransferase (QPRT) expression in the kidney facilitates resilience against acute kidney injury. *Kidney International* **104**, 1150–1163 (2023). https://doi.org/10.1016/j.kint.2023.09.013
35 Chang-Panesso, M. *et al.* FOXM1 drives proximal tubule proliferation during repair from acute ischemic kidney injury. *The Journal of Clinical Investigation* **129**, 5501–5517 (2019). https://doi.org/10.1172/JCI125519
36 Ma, H. *et al.* Dephosphorylation of AMP-activated protein kinase exacerbates ischemia/reperfusion-induced acute kidney injury via mitochondrial dysfunction. *Kidney International* **101**, 315–330 (2022). https://doi.org/10.1016/j.kint.2021.10.028
37 Havasi, A. & Borkan, S. C. Apoptosis and acute kidney injury. *Kidney International* **80**, 29–40 (2011). https://doi.org/10.1038/ki.2011.120
38 Rabb, H. *et al.* Inflammation in AKI: Current Understanding, Key Questions, and Knowledge Gaps. *Journal of the American Society of Nephrology : JASN* **27**, 371–379

(2016). https://doi.org/10.1681/ASN.2015030261
39 Fu, Y., Xiang, Y., Li, H., Chen, A. & Dong, Z. Inflammation in kidney repair: Mechanism and therapeutic potential. *Pharmacol Ther* **237**, 108240 (2022). https://doi.org/10.1016/j.pharmthera.2022.108240
40 Schödel, J. & Ratcliffe, P. J. Mechanisms of hypoxia signalling: new implications for nephrology. *Nature Reviews. Nephrology* **15**, 641–659 (2019). https://doi.org/10.1038/s41581-019-0182-z
41 Bernhardt, W. M. *et al.* Preconditional activation of hypoxia-inducible factors ameliorates ischemic acute renal failure. *Journal of the American Society of Nephrology : JASN* **17**, 1970–1978 (2006).
42 Li, Y. *et al.* Targeting the transmembrane cytokine co-receptor neuropilin-1 in distal tubules improves renal injury and fibrosis. *Nature Communications* **15**, 5731 (2024). https://doi.org/10.1038/s41467-024-50121-6
43 Ye, C., Sutter, B. M., Wang, Y., Kuang, Z. & Tu, B. P. A Metabolic Function for Phospholipid and Histone Methylation. *Molecular Cell* **66**, 180–193.e188 (2017). https://doi.org/10.1016/j.molcel.2017.02.026
44 Capelo-Diz, A. *et al.* Hepatic levels of S-adenosylmethionine regulate the adaptive response to fasting. *Cell Metabolism* **35**, 1373–1389.e1378 (2023). https://doi.org/10.1016/j.cmet.2023.07.002
45 Aissa, A. F. *et al.* Effect of methionine-deficient and methionine-supplemented diets on the hepatic one-carbon and lipid metabolism in mice. *Molecular Nutrition & Food Research* **58**, 1502–1512 (2014). https://doi.org/10.1002/mnfr.201300726
46 Li, Z. *et al.* Methionine metabolism in chronic liver diseases: an update on molecular mechanism and therapeutic implication. *Signal Transduction and Targeted Therapy* **5**, 280 (2020). https://doi.org/10.1038/s41392-020-00349-7
47 Lee, L. E., Doke, T., Mukhi, D. & Susztak, K. The key role of altered tubule cell lipid metabolism in kidney disease development. *Kidney International* **106**, 24–34 (2024). https://doi.org/10.1016/j.kint.2024.02.025
48 Rinaldi, A. *et al.* Impaired fatty acid metabolism perpetuates lipotoxicity along the transition to chronic kidney injury. *JCI Insight* **7** (2022). https://doi.org/10.1172/jci.insight.161783
49 Li, H., Dixon, E. E., Wu, H. & Humphreys, B. D. Comprehensive single-cell transcriptional profiling defines shared and unique epithelial injury responses during kidney fibrosis. *Cell Metabolism* **34**, 1977–1998.e1979 (2022). https://doi.org/10.1016/j.cmet.2022.09.026
50 Hui, S. *et al.* Quantitative Fluxomics of Circulating Metabolites. *Cell Metab* **32**, 676–688 e674 (2020). https://doi.org/10.1016/j.cmet.2020.07.013
51 Bornstein, M. R. *et al.* Comprehensive quantification of metabolic flux during acute cold stress in mice. *Cell Metabolism* **35**, 2077–2092.e2076 (2023). https://doi.org/10.1016/j.cmet.2023.09.002
52 Ghergurovich, J. M. *et al.* Methionine synthase supports tumour tetrahydrofolate pools. *Nature Metabolism* **3**, 1512–1520 (2021). https://doi.org/10.1038/s42255-021-00465-w
53 Hui, S. *et al.* Glucose feeds the TCA cycle via circulating lactate. *Nature* **551**, 115–118

(2017). https://doi.org/10.1038/nature24057
54 Bartman, C. R. *et al.* Slow TCA flux and ATP production in primary solid tumours but not metastases. *Nature* **614**, 349–357 (2023). https://doi.org/10.1038/s41586-022-05661-6
55 Matsuura, R., Doi, K. & Rabb, H. Acute kidney injury and distant organ dysfunction–network system analysis. *Kidney International* **103**, 1041–1055 (2023). https://doi.org/10.1016/j.kint.2023.03.025
56 Perner, A. *et al.* Fluid management in acute kidney injury. *Intensive Care Medicine* **43**, 807–815 (2017). https://doi.org/10.1007/s00134-017-4817-x
57 Bezwada, D. *et al.* Mitochondrial complex I promotes kidney cancer metastasis. *Nature* **633**, 923–931 (2024). https://doi.org/10.1038/s41586-024-07812-3
58 Bonventre, J. V. & Yang, L. Cellular pathophysiology of ischemic acute kidney injury. *Journal of Clinical Investigation* **121**, 4210–4221 (2011). https://doi.org/10.1172/jci45161
59 Cooke, D., Ouattara, A. & Ables, G. P. Dietary methionine restriction modulates renal response and attenuates kidney injury in mice. *The FASEB Journal* **32**, 693–702 (2018). https://doi.org/10.1096/fj.201700419R
60 Ramalingam, H. *et al.* A methionine-Mettl3-N(6)-methyladenosine axis promotes polycystic kidney disease. *Cell Metab* (2021). https://doi.org/10.1016/j.cmet.2021.03.024
61 Fang, H., Stone, K. P., Wanders, D., Forney, L. A. & Gettys, T. W. The Origins, Evolution, and Future of Dietary Methionine Restriction. *Annual Review of Nutrition* **42**, 201–226 (2022). https://doi.org/10.1146/annurev-nutr-062320-111849
62 Plaisance, E. P. *et al.* Dietary methionine restriction increases fat oxidation in obese adults with metabolic syndrome. *J Clin Endocrinol Metab* **96**, E836–E840 (2011). https://doi.org/10.1210/jc.2010-2493
63 Hasek, B. E. *et al.* Dietary methionine restriction enhances metabolic flexibility and increases uncoupled respiration in both fed and fasted states. *Am J Physiol Regul Integr Comp Physiol* **299**, R728–R739 (2010). https://doi.org/10.1152/ajpregu.00837.2009
64 Varkaneh Kord, H. *et al.* The influence of fasting and energy-restricted diets on leptin and adiponectin levels in humans: A systematic review and meta-analysis. *Clinical Nutrition (Edinburgh, Scotland)* **40**, 1811–1821 (2021). https://doi.org/10.1016/j.clnu.2020.10.034
65 Travers, R. L., Trim, W. V., Motta, A. C., Betts, J. A. & Thompson, D. Calorie restriction-induced leptin reduction and T-lymphocyte activation in blood and adipose tissue in men with overweight and obesity. *Int J Obes (Lond)* **48** (2024). https://doi.org/10.1038/s41366-024-01513-7
66 Green, C. L., Lamming, D. W. & Fontana, L. Molecular mechanisms of dietary restriction promoting health and longevity. *Nat Rev Mol Cell Biol* **23**, 56–73 (2022). https://doi.org/10.1038/s41580-021-00411-4
67 Wang, S.-Y. *et al.* Methionine restriction delays senescence and suppresses the senescence-associated secretory phenotype in the kidney through endogenous hydrogen sulfide. *Cell Cycle* **18**, 1573–1587 (2019). https://doi.org/10.1080/15384101.2019.1618124
68 Grant, L. *et al.* Methionine restriction improves renal insulin signalling in aged kidneys.

Mech Ageing Dev **157**, 35–43 (2016). https://doi.org/10.1016/j.mad.2016.07.003

69 Oh, C. J. *et al.* Inhibition of pyruvate dehydrogenase kinase 4 ameliorates kidney ischemia-reperfusion injury by reducing succinate accumulation during ischemia and preserving mitochondrial function during reperfusion. *Kidney International* **104**, 724–739 (2023). https://doi.org/10.1016/j.kint.2023.06.022

70 Chao, E. C. & Henry, R. R. SGLT2 inhibition--a novel strategy for diabetes treatment. *Nature Reviews. Drug Discovery* **9**, 551–559 (2010). https://doi.org/10.1038/nrd3180

71 Palmer, B. F. & Clegg, D. J. Euglycemic Ketoacidosis as a Complication of SGLT2 Inhibitor Therapy. *Clinical Journal of the American Society of Nephrology : CJASN* **16**, 1284–1291 (2021). https://doi.org/10.2215/CJN.17621120

72 Palmer, B. F. & Clegg, D. J. Starvation Ketosis and the Kidney. *American Journal of Nephrology* **52**, 467–478 (2021). https://doi.org/10.1159/000517305

73 Daniele, G. *et al.* Dapagliflozin Enhances Fat Oxidation and Ketone Production in Patients With Type 2 Diabetes. *Diabetes Care* **39**, 2036–2041 (2016).

74 Ferrannini, E. *et al.* Shift to Fatty Substrate Utilization in Response to Sodium-Glucose Cotransporter 2 Inhibition in Subjects Without Diabetes and Patients With Type 2 Diabetes. *Diabetes* **65**, 1190–1195 (2016). https://doi.org/10.2337/db15-1356

75 Palmer, B. F. & Clegg, D. J. Kidney-Protective Effects of SGLT2 Inhibitors. *Clinical Journal of the American Society of Nephrology : CJASN* **18**, 279–289 (2022). https://doi.org/10.2215/CJN.09380822

76 Mentch, S. J. *et al.* Histone Methylation Dynamics and Gene Regulation Occur through the Sensing of One-Carbon Metabolism. *Cell metabolism* **22**, 861–873 (2015). https://doi.org/10.1016/j.cmet.2015.08.024

77 Sutter, B. M., Wu, X., Laxman, S. & Tu, B. P. Methionine inhibits autophagy and promotes growth by inducing the SAM-responsive methylation of PP2A. *Cell* **154**, 403–415 (2013). https://doi.org/10.1016/j.cell.2013.06.041

78 Laxman, S. *et al.* Sulfur amino acids regulate translational capacity and metabolic homeostasis through modulation of tRNA thiolation. *Cell* **154**, 416–429 (2013). https://doi.org/10.1016/j.cell.2013.06.043

79 Ji, M. *et al.* Methionine restriction-induced sulfur deficiency impairs antitumour immunity partially through gut microbiota. *Nat Metab* **5**, 1526–1543 (2023). https://doi.org/10.1038/s42255-023-00854-3

80 Fang, W. *et al.* Methionine restriction constrains lipoylation and activates mitochondria for nitrogenic synthesis of amino acids. *Nature communications* **14**, 2504 (2023). https://doi.org/10.1038/s41467-023-38289-9

81 Xue, J. & Ye, C. The role of lipoylation in mitochondrial adaptation to methionine restriction. *Bioessays* **46**, e2300218 (2024). https://doi.org/10.1002/bies.202300218

82 Zou, K. *et al.* Life span extension by glucose restriction is abrogated by methionine supplementation: Cross-talk between glucose and methionine and implication of methionine as a key regulator of life span. *Sci Adv* **6**, eaba1306 (2020). https://doi.org/10.1126/sciadv.aba1306

83 Ostermann, M., Straaten, H. M. O.-v. & Forni, L. G. Fluid overload and acute kidney injury: cause or consequence? *Critical Care (London, England)* **19**, 443 (2015). https://doi.org/10.1186/s13054-015-1163-7

84 Bouchard, J. *et al.* Fluid accumulation, survival and recovery of kidney function in critically ill patients with acute kidney injury. *Kidney International* **76**, 422–427 (2009). https://doi.org/10.1038/ki.2009.159

85 Faubel, S. & Edelstein, C. L. Mechanisms and mediators of lung injury after acute kidney injury. *Nature Reviews. Nephrology* **12**, 48–60 (2016). https://doi.org/10.1038/nrneph.2015.158

86 Matsuura, R., Doi, K. & Rabb, H. Acute kidney injury and distant organ dysfunction-network system analysis. *Kidney International* **103**, 1041–1055 (2023). https://doi.org/10.1016/j.kint.2023.03.025

87 Wei, Q. Q. & Dong, Z. Mouse model of ischemic acute kidney injury: technical notes and tricks. *American Journal of Physiology-Renal Physiology* **303**, F1487–F1494 (2012). https://doi.org/10.1152/ajprenal.00352.2012

88 Lin, K. *et al.* Disrupted methionine cycle triggers muscle atrophy in cancer cachexia through epigenetic regulation of REDD1. *Cell Metabolism* **37** (2025). https://doi.org/10.1016/j.cmet.2024.10.017

89 Durie, D., McDonald, T. S. & Borges, K. The effect of dichloroacetate in mouse models of epilepsy. *Epilepsy Res* **145**, 77–81 (2018). https://doi.org/10.1016/j.eplepsyres.2018.06.004

90 Kellum, J. A. *et al.* Kidney disease: improving global outcomes (KDIGO) acute kidney injury work group. KDIGO clinical practice guideline for acute kidney injury. **2**, 1–138 (2012).

91 Singer, M. *et al.* The Third International Consensus Definitions for Sepsis and Septic Shock (Sepsis-3). *JAMA* **315**, 801–810 (2016). https://doi.org/10.1001/jama.2016.0287

92 Fang, W. *et al.* Methionine restriction constrains lipoylation and activates mitochondria for nitrogenic synthesis of amino acids. *Nature Communications* **14** (2023). https://doi.org/10.1038/s41467-023-38289-9

93 Yuan, M., Breitkopf, S. B., Yang, X. & Asara, J. M. A positive/negative ion-switching, targeted mass spectrometry-based metabolomics platform for bodily fluids, cells, and fresh and fixed tissue. *Nature Protocols* **7**, 872–881 (2012). https://doi.org/10.1038/nprot.2012.024

94 Zhou, Y. *et al.* Metascape provides a biologist-oriented resource for the analysis of systems-level datasets. *Nature Communications* **10**, 1523 (2019). https://doi.org/10.1038/s41467-019-09234-6

95 Pang, Z. *et al.* MetaboAnalyst 6.0: towards a unified platform for metabolomics data processing, analysis and interpretation. *Nucleic Acids Research* **52**, W398–W406 (2024). https://doi.org/10.1093/nar/gkae253

96 Wu, T. *et al.* clusterProfiler 4.0: A universal enrichment tool for interpreting omics data. *Innovation (Camb)* **2**, 100141 (2021). https://doi.org/10.1016/j.xinn.2021.100141

97 Ewald, J. D. *et al.* Web-based multi-omics integration using the Analyst software suite. *Nature Protocols* (2024). https://doi.org/10.1038/s41596-023-00950-4
98 Heinrich, P. *et al.* Correcting for natural isotope abundance and tracer impurity in MS-, MS/MS- and high-resolution-multiple-tracer-data from stable isotope labeling experiments with IsoCorrectoR. *Scientific Reports* **8**, 17910 (2018). https://doi.org/10.1038/s41598-018-36293-4
99 Kreuzaler, P. *et al.* Vitamin B5 supports MYC oncogenic metabolism and tumor progression in breast cancer. *Nature Metabolism* **5**, 1870–1886 (2023). https://doi.org/10.1038/s42255-023-00915-7
100 Zhang, D. *et al.* Tubular p53 regulates multiple genes to mediate AKI. *Journal of the American Society of Nephrology : JASN* **25**, 2278–2289 (2014). https://doi.org/10.1681/ASN.2013080902
101 Mehlem, A., Hagberg, C. E., Muhl, L., Eriksson, U. & Falkevall, A. Imaging of neutral lipids by oil red O for analyzing the metabolic status in health and disease. *Nature Protocols* **8**, 1149–1154 (2013). https://doi.org/10.1038/nprot.2013.055
102 Yang, S., Xue, J. & Ye, C. Protocol for rapid and accurate quantification of phospholipids in yeast and mammalian systems using LC-MS. *STAR Protoc* **3**, 101769 (2022). https://doi.org/10.1016/j.xpro.2022.101769
103 Zhu, Y. *et al.* Phospholipid biosynthesis modulates nucleotide metabolism and reductive capacity. *Nature Chemical Biology* (2024). https://doi.org/10.1038/s41589-024-01689-z

Acknowledgments

We thank technical support from the Core Facility of Life Sciences Institute, Zhejiang University. We thank Q. Huang, C. Zhang, and J. Chen from the Core Facilities, Zhejiang University School of Medicine for their technical support. We are grateful for the technical assistance with TEM provided J. Li, and H. Qian of the analysis center of the Analysis Center of Agrobiology and Environmental Sciences of Zhejiang University. We also thank X. Wang of the Institute of Immunology, Zhejiang University School of Medicine, for generously providing the PEMT antibody. This work was supported by grants from the National Key Research and Development Program of China (2023YFA1801100 and 2024YFA1803000), the National Natural Science Foundation of China (32270816 and 92057102), Double Thousand Plan of Jiangxi Province (jxsq2023102239), the Fundamental Research Funds for the Central Universities (226-2024-00088), the startup fund from the Life Sciences Institute of Zhejiang University, and the 1000 Talents Program for Young Scholars to C.Y. and the Huadong Medicine Joint Funds of the Zhejiang Provincial Natural Science Foundation of China (LHDMZ23H100001) and Natural Science Foundation of China (U21A20350, 82070729, 82471713) to H.J.

Competing interests

The authors declare no competing interests.

Supplementary information

Supplementary Information

Supplementary Data 1

Supplementary Data 2

Author contributions

Conceptualization: C.Y., X.P., and H.J.; Methodology: X.P., Y.X., and C.Y.; Investigation: X.P., Y.X., H.P., T.M., Y.Z., and Q.S; Visualization: X.P. and Y.X.; Supervision: C.Y., H.J., and J.C.; Writing: X.P. and C.Y.; Funding acquisition: C.Y. and H.J.; Project administration: C.Y. All authors read, edited, and approved the manuscript. X.P. and Y.X. contributed equally to this work.

Editor's Summary

Multi-omic profiling demonstrates that short-term methionine deprivation in mice lowers S-adenosylmethionine levels, boosting kidney protection against ischemia–reperfusion injury by enhancing glucose oxidation via increased pyruvate dehydrogenase activity.

Peer review statement

Communications Biology thanks Kumiko Torisu and Ton Rabelink for their contribution to the peer review of this work. Primary Handling Editor: Dario Ummarino. A peer review file is available.

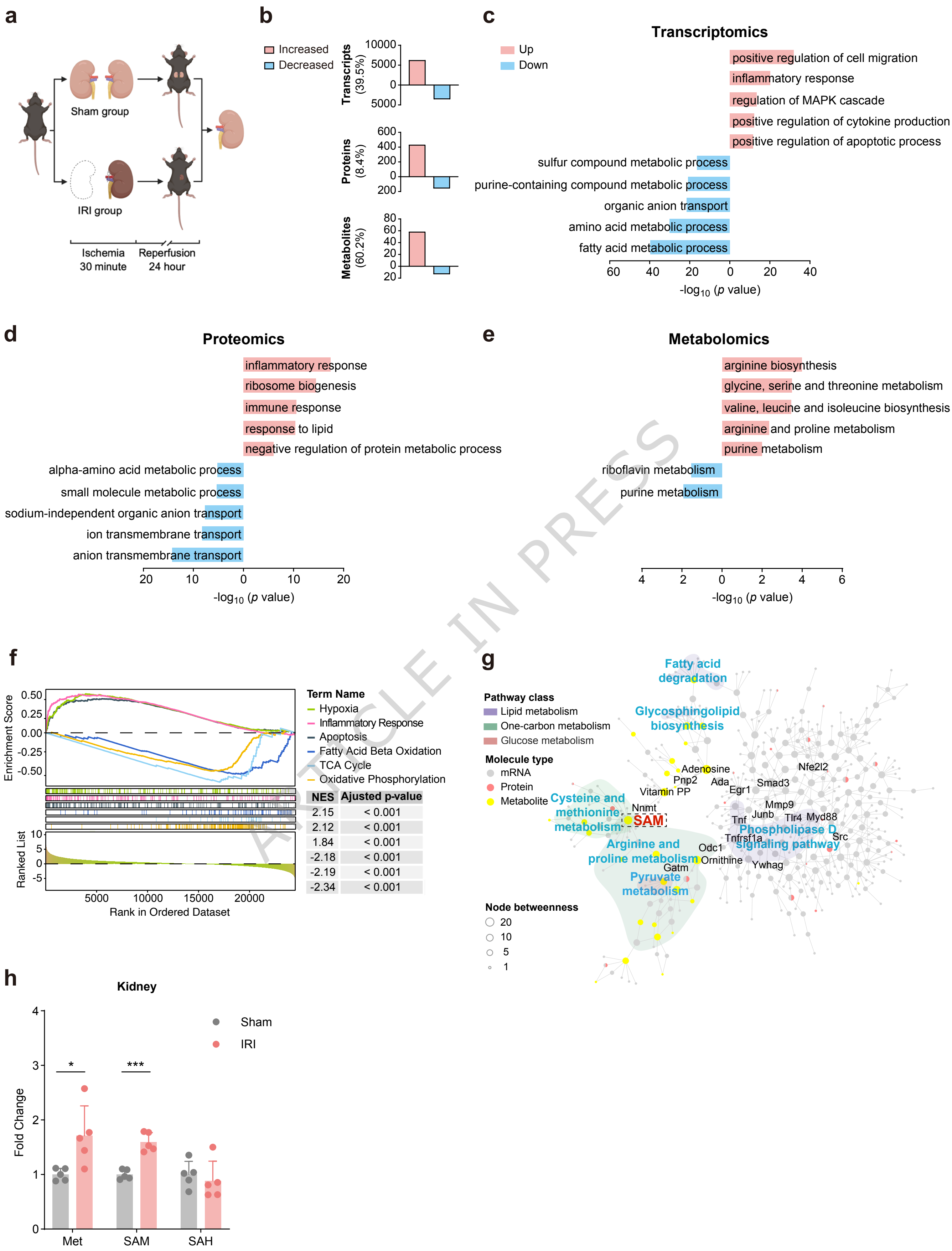
a
Sham group
IRI group
Ischemia
30 minute
Reperfusion
24 hour
b
Increased
Decreased
Transcripts (39.5%)
Proteins (8.4%)
Metabolites (60.2%)
c
Transcriptomics
Up
Down
positive regulation of cell migration
inflammatory response
regulation of MAPK cascade
positive regulation of cytokine production
positive regulation of apoptotic process
sulfur compound metabolic process
purine-containing compound metabolic process
organic anion transport
amino acid metabolic process
fatty acid metabolic process
-log10 (p value)
d
Proteomics
inflammatory response
ribosome biogenesis
immune response
response to lipid
negative regulation of protein metabolic process
alpha-amino acid metabolic process
small molecule metabolic process
sodium-independent organic anion transport
ion transmembrane transport
anion transmembrane transport
-log10 (p value)
e
Metabolomics
arginine biosynthesis
glycine, serine and threonine metabolism
valine, leucine and isoleucine biosynthesis
arginine and proline metabolism
purine metabolism
riboflavin metabolism
purine metabolism
-log10 (p value)
f
Enrichment Score
Ranked List
Rank in Ordered Dataset
Term Name
Hypoxia
Inflammatory Response
Apoptosis
Fatty Acid Beta Oxidation
TCA Cycle
Oxidative Phosphorylation
NES Ajusted p-value
2.15 < 0.001
2.12 < 0.001
1.84 < 0.001
-2.18 < 0.001
-2.19 < 0.001
-2.34 < 0.001
g
Pathway class
Lipid metabolism
One-carbon metabolism
Glucose metabolism
Molecule type
mRNA
Protein
Metabolite
Node betweenness
Fatty acid degradation
Glycosphingolipid biosynthesis
Cysteine and methionine metabolism
SAM
Arginine and proline metabolism
Pyruvate metabolism
Phospholipase D signaling pathway
Adenosine
Pnp2
Ada
Vitamin PP
Nnmt
Egr1
Smad3
Nfe2l2
Mmp9
Tnf
Junb
Tlr4
Myd88
Tnfrsf1a
Src
Odc1
Ornithine
Gatm
Ywhag
h
Kidney
Sham
IRI
Fold Change
Met
SAM
SAH

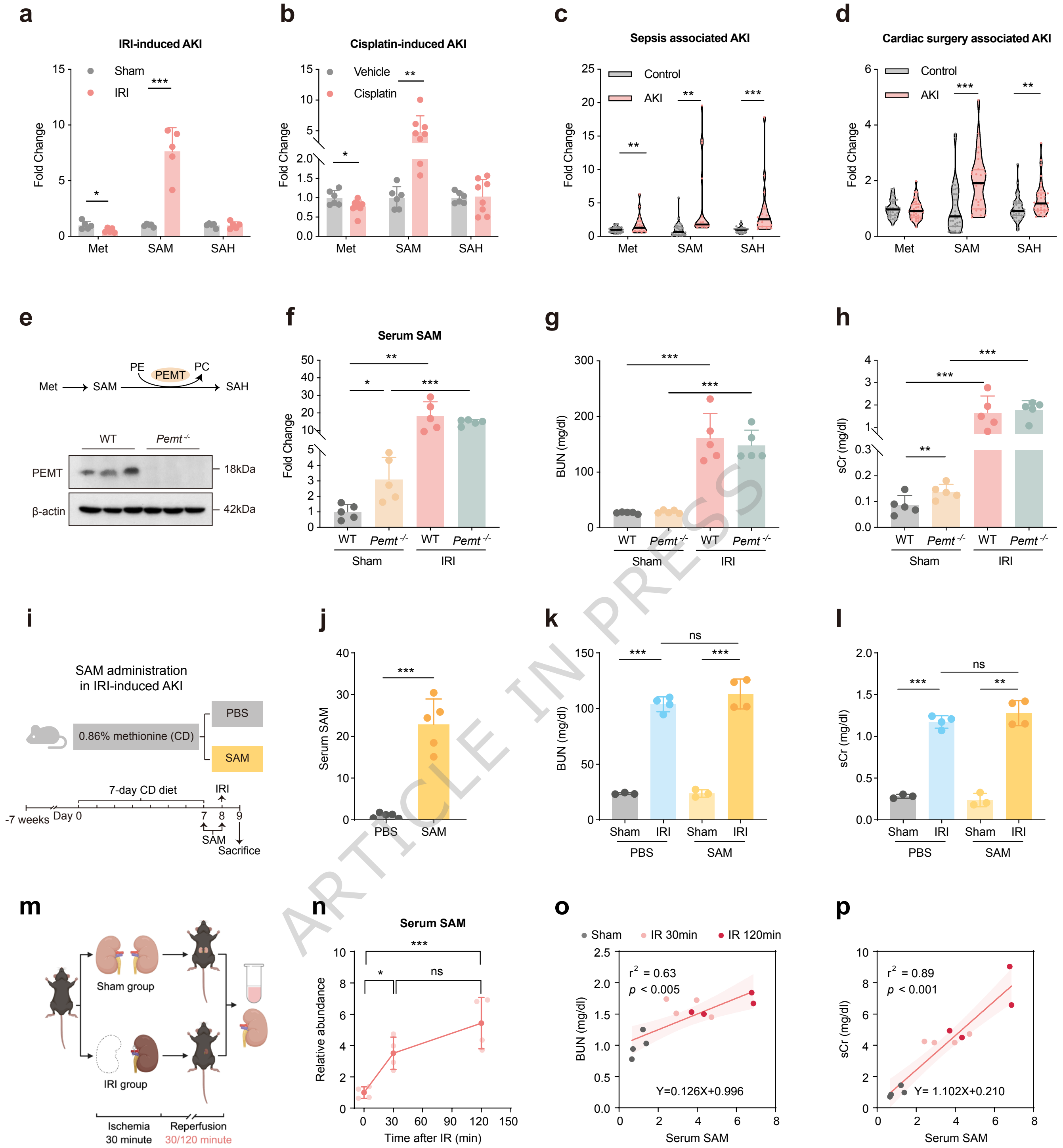
a
IRI-induced AKI
Sham
IRI
Fold Change
Met
SAM
SAH
b
Cisplatin-induced AKI
Vehicle
Cisplatin
Fold Change
Met
SAM
SAH
c
Sepsis associated AKI
Control
AKI
Fold Change
Met
SAM
SAH
d
Cardiac surgery associated AKI
Control
AKI
Fold Change
Met
SAM
SAH
e
PE
PEMT
PC
Met
SAM
SAH
WT
Pemt-/-
PEMT
β-actin
18kDa
42kDa
f
Serum SAM
Fold Change
WT
Pemt-/-
Sham
IRI
g
BUN (mg/dl)
WT
Pemt-/-
Sham
IRI
h
sCr (mg/dl)
WT
Pemt-/-
Sham
IRI
i
SAM administration
in IRI-induced AKI
0.86% methionine (CD)
PBS
SAM
7-day CD diet
IRI
-7 weeks
Day 0
7
8
9
SAM
Sacrifice
j
Serum SAM
PBS
SAM
k
BUN (mg/dl)
ns
Sham
IRI
PBS
SAM
l
sCr (mg/dl)
ns
Sham
IRI
PBS
SAM
m
Sham group
IRI group
Ischemia
30 minute
Reperfusion
30/120 minute
n
Serum SAM
ns
Relative abundance
Time after IR (min)
o
Sham
IR 30min
IR 120min
r2 = 0.63
p < 0.005
Y=0.126X+0.996
BUN (mg/dl)
Serum SAM
p
r2 = 0.89
p < 0.001
Y= 1.102X+0.210
sCr (mg/dl)
Serum SAM

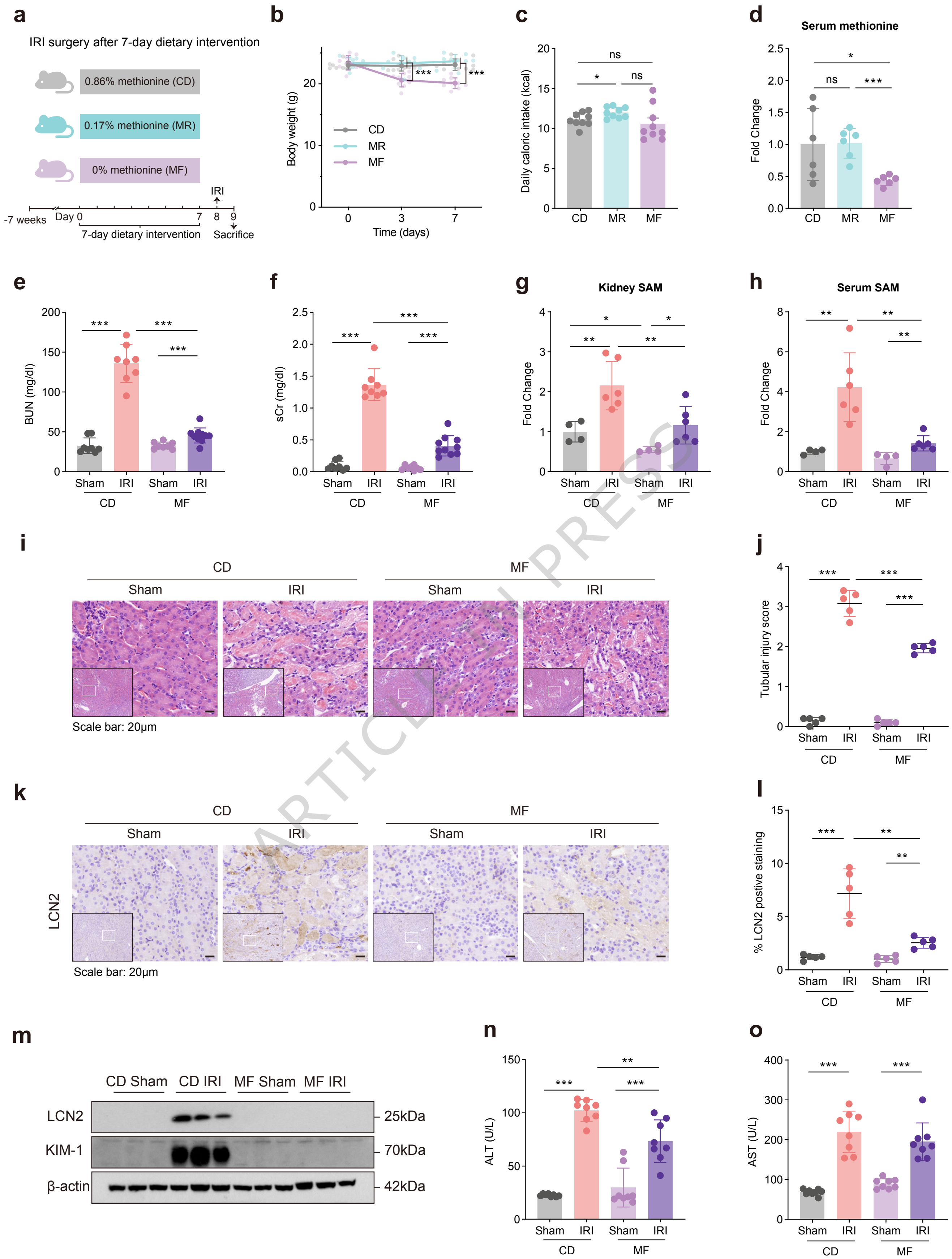
a
IRI surgery after 7-day dietary intervention
0.86% methionine (CD)
0.17% methionine (MR)
0% methionine (MF)
IRI
-7 weeks
Day 0
7
8
9
7-day dietary intervention
Sacrifice
b
Body weight (g)
Time (days)
CD
MR
MF
***
c
Daily caloric intake (kcal)
ns
*
CD
MR
MF
d
Serum methionine
Fold Change
ns
*
***
CD
MR
MF
e
BUN (mg/dl)
f
sCr (mg/dl)
g
Kidney SAM
Fold Change
h
Serum SAM
Fold Change
Sham
IRI
CD
MF
i
Scale bar: 20μm
j
Tubular injury score
k
LCN2
Scale bar: 20μm
l
% LCN2 postive staining
m
CD Sham
CD IRI
MF Sham
MF IRI
LCN2
KIM-1
β-actin
25kDa
70kDa
42kDa
n
ALT (U/L)
o
AST (U/L)

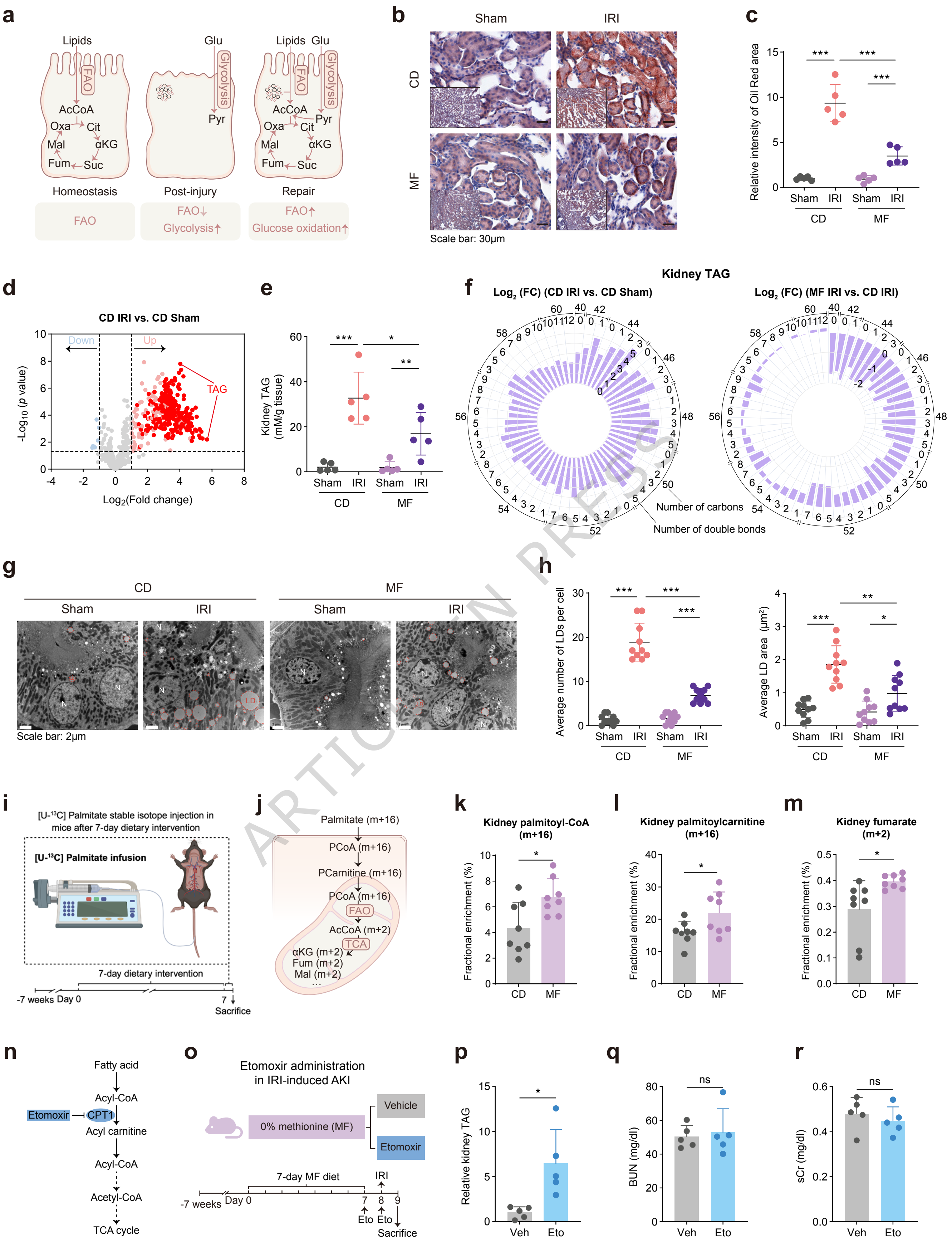
a
Lipids
Glu
Lipids Glu
FAO
Glycolysis
AcCoA
Oxa
Cit
Mal
αKG
Fum
Suc
Pyr
Homeostasis
Post-injury
Repair
FAO
FAO↓
Glycolysis↑
FAO↑
Glucose oxidation↑
b
Sham
IRI
CD
MF
Scale bar: 30μm
c
Relative intensity of Oil Red area
Sham IRI Sham IRI
CD MF
d
CD IRI vs. CD Sham
Down
Up
TAG
-Log10 (p value)
Log2(Fold change)
e
Kidney TAG (mM/g tissue)
Sham IRI Sham IRI
CD MF
f
Kidney TAG
Log2 (FC) (CD IRI vs. CD Sham)
Log2 (FC) (MF IRI vs. CD IRI)
Number of carbons
Number of double bonds
g
CD
MF
Sham
IRI
Sham
IRI
LD
N
Scale bar: 2μm
h
Average number of LDs per cell
Average LD area (μm²)
Sham IRI Sham IRI
CD MF
i
[U-¹³C] Palmitate stable isotope injection in mice after 7-day dietary intervention
[U-¹³C] Palmitate infusion
7-day dietary intervention
-7 weeks Day 0
7
Sacrifice
j
Palmitate (m+16)
PCoA (m+16)
PCarnitine (m+16)
PCoA (m+16)
FAO
AcCoA (m+2)
TCA
αKG (m+2)
Fum (m+2)
Mal (m+2)
k
Kidney palmitoyl-CoA (m+16)
l
Kidney palmitoylcarnitine (m+16)
m
Kidney fumarate (m+2)
Fractional enrichment (%)
CD MF
n
Fatty acid
Acyl-CoA
Etomoxir
CPT1
Acyl carnitine
Acyl-CoA
Acetyl-CoA
TCA cycle
o
Etomoxir administration in IRI-induced AKI
0% methionine (MF)
Vehicle
Etomoxir
7-day MF diet
IRI
-7 weeks Day 0
7 8 9
Eto Eto
Sacrifice
p
Relative kidney TAG
q
BUN (mg/dl)
r
sCr (mg/dl)
Veh Eto
ns

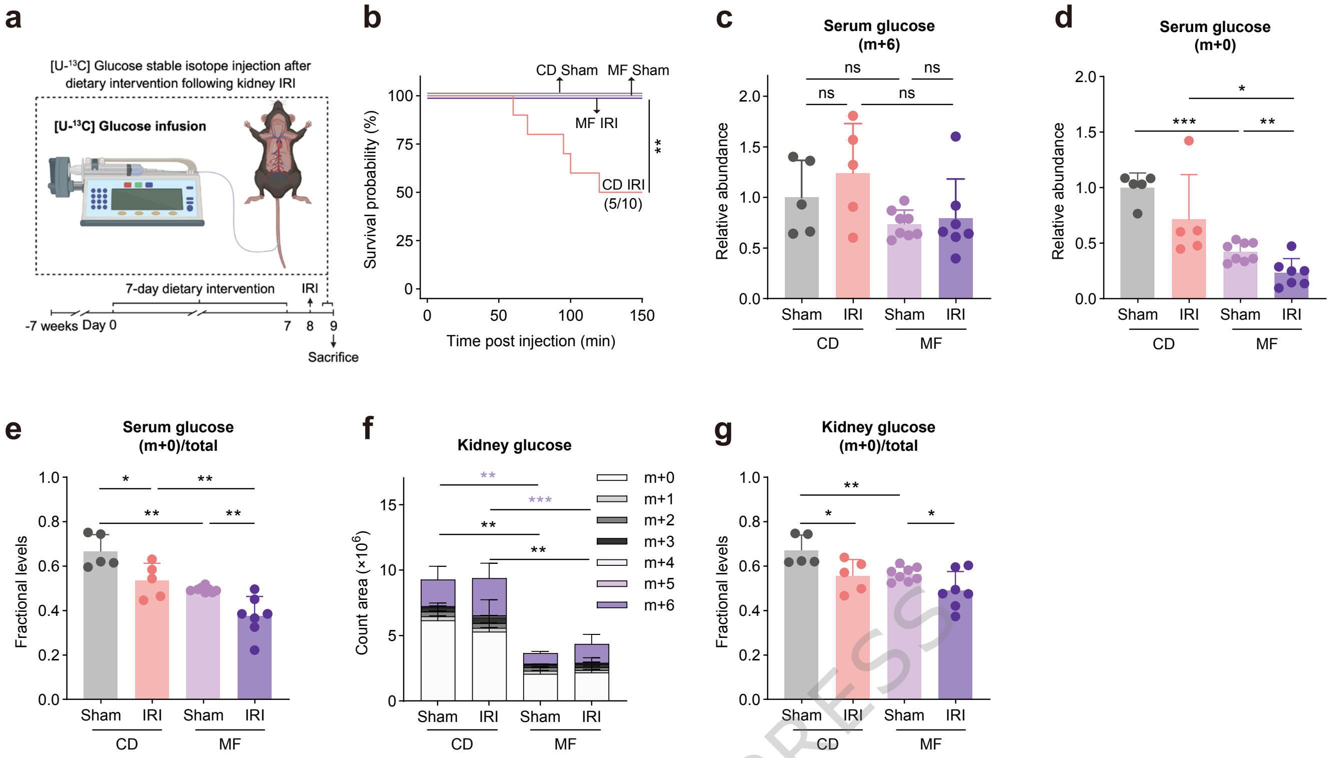
a
[U-13C] Glucose stable isotope injection after dietary intervention following kidney IRI
[U-13C] Glucose infusion
7-day dietary intervention
IRI
-7 weeks
Day 0
7
8
9
Sacrifice
b
CD Sham
MF Sham
MF IRI
CD IRI
(5/10)
**
Survival probability (%)
Time post injection (min)
c
Serum glucose (m+6)
ns
Relative abundance
Sham
IRI
CD
MF
d
Serum glucose (m+0)
***
**
*
Relative abundance
e
Serum glucose (m+0)/total
Fractional levels
f
Kidney glucose
m+0
m+1
m+2
m+3
m+4
m+5
m+6
Count area (×10⁶)
g
Kidney glucose (m+0)/total
Fractional levels

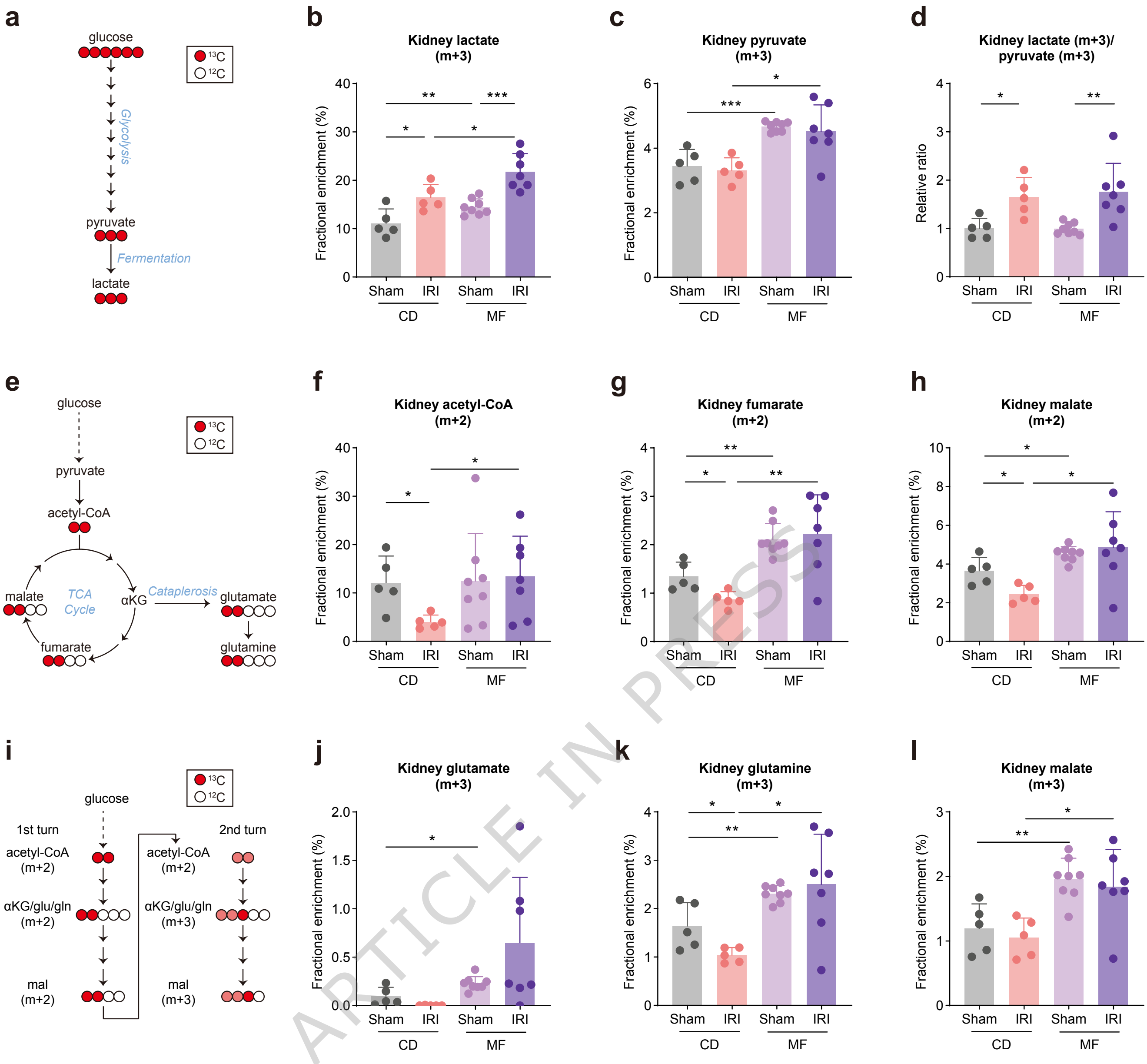
a
glucose
13C
12C
Glycolysis
pyruvate
Fermentation
lactate
b
Kidney lactate (m+3)
Fractional enrichment (%)
Sham
IRI
Sham
IRI
CD
MF
c
Kidney pyruvate (m+3)
d
Kidney lactate (m+3)/ pyruvate (m+3)
Relative ratio
e
glucose
pyruvate
acetyl-CoA
TCA Cycle
malate
αKG
Cataplerosis
glutamate
fumarate
glutamine
f
Kidney acetyl-CoA (m+2)
g
Kidney fumarate (m+2)
h
Kidney malate (m+2)
i
glucose
1st turn
2nd turn
acetyl-CoA (m+2)
αKG/glu/gln (m+2)
αKG/glu/gln (m+3)
mal (m+2)
mal (m+3)
j
Kidney glutamate (m+3)
k
Kidney glutamine (m+3)
l
Kidney malate (m+3)

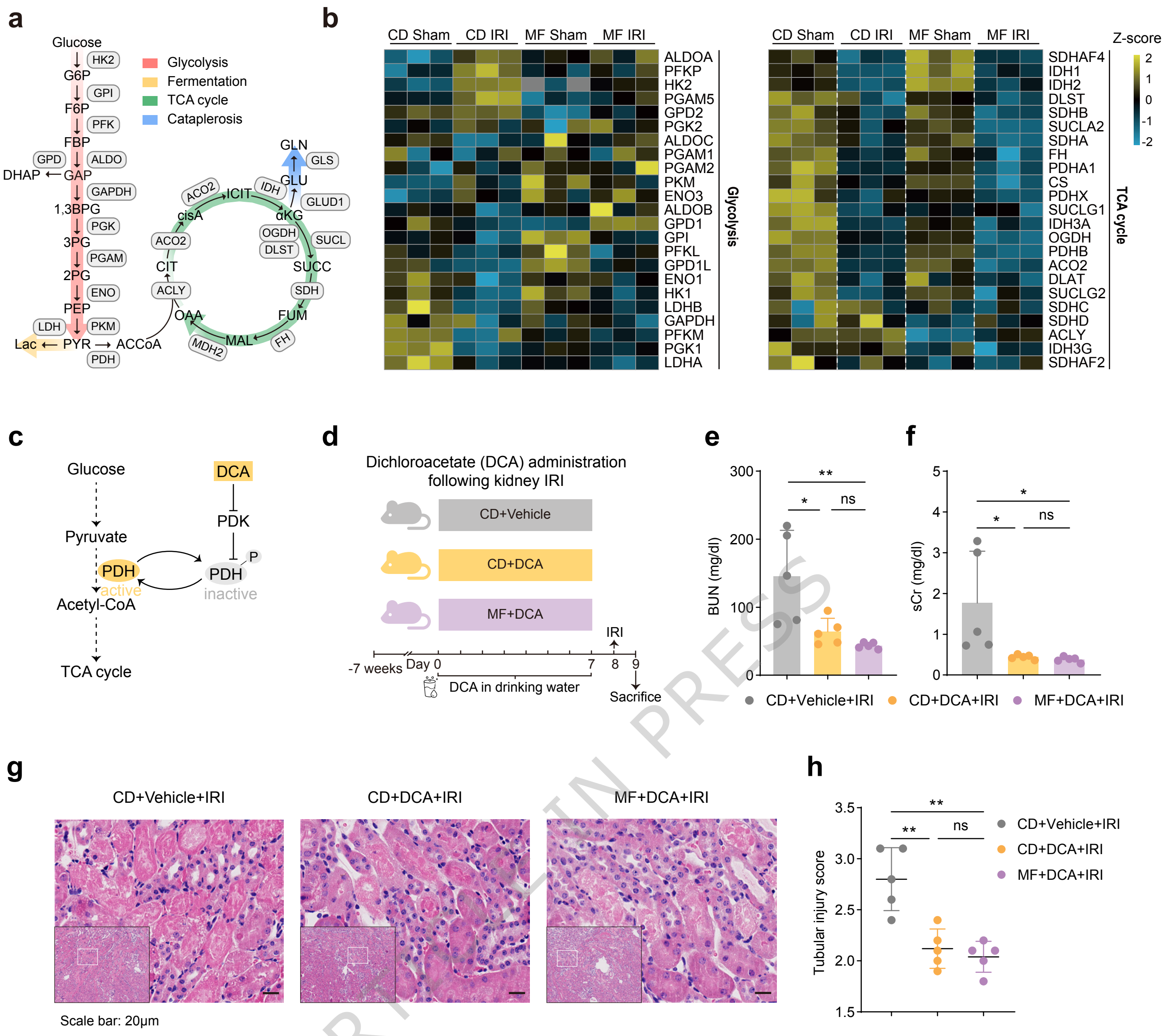
a
Glucose
HK2
G6P
GPI
F6P
PFK
FBP
GPD
ALDO
DHAP
GAP
GAPDH
1,3BPG
PGK
3PG
PGAM
2PG
ENO
PEP
LDH
PKM
Lac
PYR
ACCoA
PDH
Glycolysis
Fermentation
TCA cycle
Cataplerosis
GLN
GLS
GLU
GLUD1
ACO2
ICIT
IDH
cisA
αKG
OGDH
DLST
SUCL
SUCC
SDH
FUM
FH
MAL
MDH2
OAA
ACLY
CIT
b
CD Sham
CD IRI
MF Sham
MF IRI
ALDOA
PFKP
HK2
PGAM5
GPD2
PGK2
ALDOC
PGAM1
PGAM2
PKM
ENO3
ALDOB
GPD1
GPI
PFKL
GPD1L
ENO1
HK1
LDHB
GAPDH
PFKM
PGK1
LDHA
Glycolysis
SDHAF4
IDH1
IDH2
DLST
SDHB
SUCLA2
SDHA
FH
PDHA1
CS
PDHX
SUCLG1
IDH3A
OGDH
PDHB
ACO2
DLAT
SUCLG2
SDHC
SDHD
ACLY
IDH3G
SDHAF2
TCA cycle
Z-score
2
1
0
-1
-2
c
Glucose
DCA
PDK
Pyruvate
PDH
active
PDH
inactive
P
Acetyl-CoA
TCA cycle
d
Dichloroacetate (DCA) administration
following kidney IRI
CD+Vehicle
CD+DCA
MF+DCA
IRI
-7 weeks
Day 0
7
8
9
DCA in drinking water
Sacrifice
e
BUN (mg/dl)
300
200
100
0
**
*
ns
f
sCr (mg/dl)
5
4
3
2
1
0
*
*
ns
CD+Vehicle+IRI
CD+DCA+IRI
MF+DCA+IRI
g
CD+Vehicle+IRI
CD+DCA+IRI
MF+DCA+IRI
Scale bar: 20μm
h
Tubular injury score
3.5
3.0
2.5
2.0
1.5
**
**
ns
CD+Vehicle+IRI
CD+DCA+IRI
MF+DCA+IRI

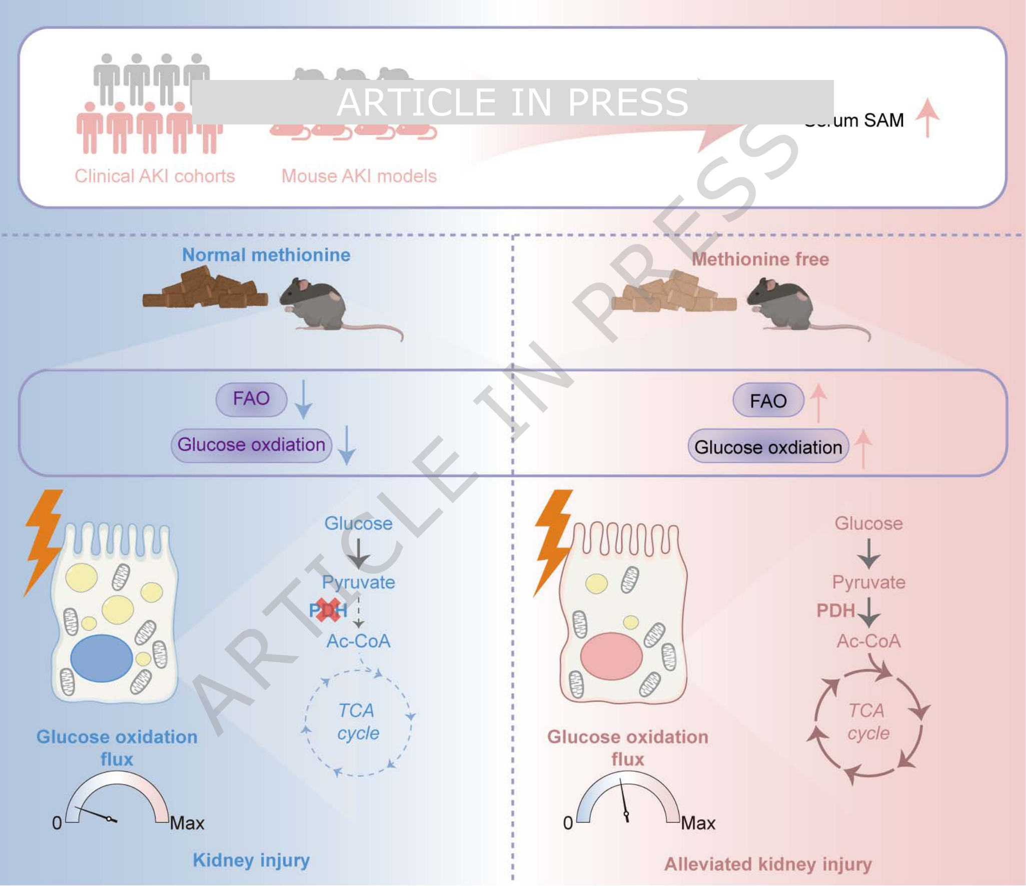
Clinical AKI cohorts
Mouse AKI models
Normal methionine
Methionine free
FAO
Glucose oxdiation
FAO
Glucose oxdiation
Glucose
Pyruvate
PDH
Ac-CoA
TCA cycle
Glucose oxidation flux
0
Max
Kidney injury
Glucose
Pyruvate
PDH
Ac-CoA
TCA cycle
Glucose oxidation flux
0
Max
Alleviated kidney injury